Space Sci Rev (2016) 199:689–719
DOI 10.1007/s11214-014-0127-6

Mission Oriented Support and Theory (MOST) for MMS—the Goddard Space Flight Center/University of California Los Angeles Interdisciplinary Science Program

Melvyn L. Goldstein · Maha Ashour-Abdalla · Adolfo F. Viñas · John Dorelli · Deirdre Wendel · Alex Klimas · Kyoung-Joo Hwang · Mostafa El-Alaoui · Raymond J. Walker · Qingjiang Pan · Haoming Liang

Received: 6 March 2014 / Accepted: 9 December 2014 / Published online: 13 January 2015

Abstract The *MOST* IDS team was tasked with focusing on two general areas: The first was to participate with the Fast Plasma Investigation (FPI) team in the development of virtual detectors that model the instrument responses of the MMS FPI sensors. The virtual instruments can be "flown through" both simulation data (from magnetohydrodynamic, hybrid, and kinetic simulations) and Cluster and THEMIS spacecraft data. The goal is to determine signatures of magnetic reconnection expected during the MMS mission. Such signatures can serve as triggers for selection of burst mode downloads. The chapter contributed by the FPI team covers that effort in detail and, therefore, most of that work has not been included here. The second area of emphasis, and the one detailed in this chapter, was to build on past and present knowledge of magnetic reconnection and its physical signatures. Below we describe intensive analyses of Cluster and THEMIS data together with theoretical models and simulations that delineate the plasma signatures that surround sites of reconnection, including the effects of turbulence as well as the detailed kinetic signatures that indicate proximity to reconnection sites. In particular, we point out that particles are energized in several regions, not only at the actual site of reconnection.

Keywords Magnetic reconnection · Plasma physics · Magnetofluid turbulence

M.L. Goldstein (✉) · M. Ashour-Abdalla · A.F. Viñas · J. Dorelli · D. Wendel · A. Klimas · K.-J. Hwang
NASA Goddard Space Flight Center, Greenbelt, MD, USA
e-mail: melvyn.l.goldstein@nasa.gov

M. Ashour-Abdalla · M. El-Alaoui
Institute of Geophysics and Planetary Physics, University of California, Los Angeles, CA, USA

M. El-Alaoui · Q. Pan · H. Liang
Department of Physics and Astronomy, University of California, Los Angeles, CA, USA

R.J. Walker
Department of Earth, Planetary and Space Sciences, University of California, Los Angeles, CA, USA

A. Klimas · K.-J. Hwang
University of Maryland, Baltimore County, Baltimore, USA

1 Overview

The IDS MOST effort has had two primary areas of focus: The first is to work with the Fast Plasma Investigation (FPI) team to develop virtual-MMS FPI detectors to "fly through" both simulation data (from magnetohydrodynamic (MHD), hybrid, and kinetic simulations) and Cluster and THEMIS data to uncover signatures of magnetic reconnection that are expected to be seen during the MMS mission. Consequently, we helped in designing "burst mode triggers" to be used in selecting the highest time resolution data for download to ground. The second focus has been to build on past and present knowledge of magnetic reconnection and its physical signatures by undertaking intensive analyses of Cluster and THEMIS data, together with MHD and kinetic simulations, to delineate the plasma signatures that indicate proximity to reconnection sites. These theoretical and simulation studies have helped to clarify where particle energization that is related to magnetic reconnection is expected to occur in the magnetosphere.

Because the development of the burst mode triggers and the algorithms for computing (fluid) moments from the plasma distribution function are described in detail in the chapter contributed by the Fast Plasma Instrument team, we only very briefly mention that work. In Sect. 3 we describe work done identifying sites of reconnection on the dayside, primarily using a variety of theoretical models, simulations and Cluster data; in Sect. 4 we review similar work for magnetotail events (but now including data obtained from THEMIS). The role of turbulence in enhancing reconnection or in triggering it has been a subject of interest for many years and in Sect. 5 we review observations, simulations, and other analyses related to the relationship between turbulence and reconnection.

2 Modeling the Fast Plasma Instruments

Using simulations and current data from Cluster and THEMIS, in collaboration with the FPI team, we have constructed virtual instrument models of the FPI Dual Electron Spectrometers (DES) and Dual Ion Spectrometers (DIS) responses during encounters with expected reconnection sites in various regions of the magnetosphere. The goal has been: (1) to ensure that detectors are optimized in energy range, angular scan, and time resolution for detection of reconnection signatures; (2) to assist in the development of data analysis software and to assist in developing algorithms for computing accurate phase-space densities and plasma moments; and (3) to help in defining and refining the onboard FPI trigger algorithms needed to choose the most interesting burst mode data intervals for downlink. These activities are essential for identifying the physical processes that give rise to reconnection and that lead to heating and acceleration of ions and electrons. Both day- and night-side regions were included. The Virtual-MMS FPI detectors were designed to "fly through" data obtained from both numerical simulations and spacecraft.

The FPI/DES instrument produces 150 burst sky maps every 4.5 s and the FPI/DIS produces 30 burst sky maps every 4.5 s. One of the primary tasks of the FPI data processing unit is to evaluate in real time the data being collected by the sensors to generate trigger terms. The reader is referred to the FPI chapter for details of that aspect of our work. In addition, the computation of accurate velocity distribution functions and plasma moments requires careful error analysis to both certify the key parameters and to develop optimal schemes for in-flight calibration. The MOST team contributed to that effort, which also is summarized in the FPI chapter (and in a paper submitted to the *Journal of Geophysical Research* (Gershman et al. 2014)). That work will not be discussed further here.

3 Dayside Signatures of Reconnection

The scientific focus of MMS is to understand the physical processes that facilitate magnetic reconnection both in cases when there is a strong background field that is not reconnecting and in situations when the dominant magnetic field itself is changing direction and undergoing reconnection. The first situation—so-called *component reconnection*—is most likely to occur at the dayside magnetosheath, which MMS will encounter repeatedly during the first year of the mission. Afterwards, apogee will be increased and MMS will enter the tail plasma sheet in which the second type of geometry is found. We first describe studies focusing on the dayside and then turn to work looking at nightside phenomena.

3.1 Locating Magnetic Nulls in the Magnetosheath

One topological construct associated with magnetic reconnection is the magnetic null (see, e.g., Xiao et al. 2006; He et al. 2008 and references therein). To model an encounter with a magnetic null by MMS, we used four-point Cluster data to test techniques for detecting these three-dimensional structures in the dayside magnetosheath (Wendel and Adrian 2013). Nulls are associated with the filamentary substructure of current sheets where reconnection is occurring. In a 2D analysis, Retinò et al. (2007) found evidence for reconnection at a filamentary current layer, while Sundkvist et al. (2007) determined from structure function analyses that the field was turbulent. Wendel and Adrian (2013) showed that the Poincaré index implied that the spacecraft had encompassed a number of three-dimensional magnetic nulls, many of which were associated with strong small-scale currents. (The Poincaré index is a measure of the number of roots in a volume (Greene 1992). A root in magnetic field space corresponds to a magnetic null point in configuration space.)

In three dimensions, the reconnecting magnetic topology consists of magnetic nulls, spines, separators, and separatrices (see Wendel and Adrian 2013, for details). In strong background fields, such as will be encountered during the first year of the MMS mission, quasi-separatrix layers can take the place of separatrices and null points. As pointed out by Wendel and Adrian (2013), magnetic null points are produced in pairs of opposite polarity. A spine and a fan then define a magnetic null point. The spine consists of a field line that emanates either toward or away from a null on opposite sides of the null. The fan planes are the surface of field lines that spread away from or toward the null (see Fig. 1a in Wendel and Adrian 2013). From an eigenvalue analysis of one pair of null points, Wendel and Adrian concluded that the observed structures were spiral null points of opposite polarity that could have been topologically connected (Fig. 1). At both nulls, there was a strong current along the spine, accompanied by a more modest current perpendicular to the spine that tilted the fan toward the axis of the spine. The current along the fan was comparable to the current along the spine. At least one of the nulls exhibited a rotational, spiral flow pattern in the fan plane that was consistent with torsional spine reconnection as predicted by theory (Fig. 2). According to this model a non-ideal region about the null point creates a potential drop both parallel and perpendicular to the spine field line of the null (Parnell et al. 1996; Pontin et al. 2004, 2005, 2007, 2011; Priest and Pontin 2009). The perpendicular potential drop near the null imposes a rotational motion of fan plane field lines that have passed through the non-ideal region near the null, while an electric field parallel to the spine within the diffusion region causes a local slippage of the field lines as they rotate. The analysis provided the first *in situ* evidence for one of the null point reconnection regimes predicted in the solar corona. These results emphasize the importance of examining magnetic topology when interpreting the nature of currents and reconnection in three-dimensional turbulence.

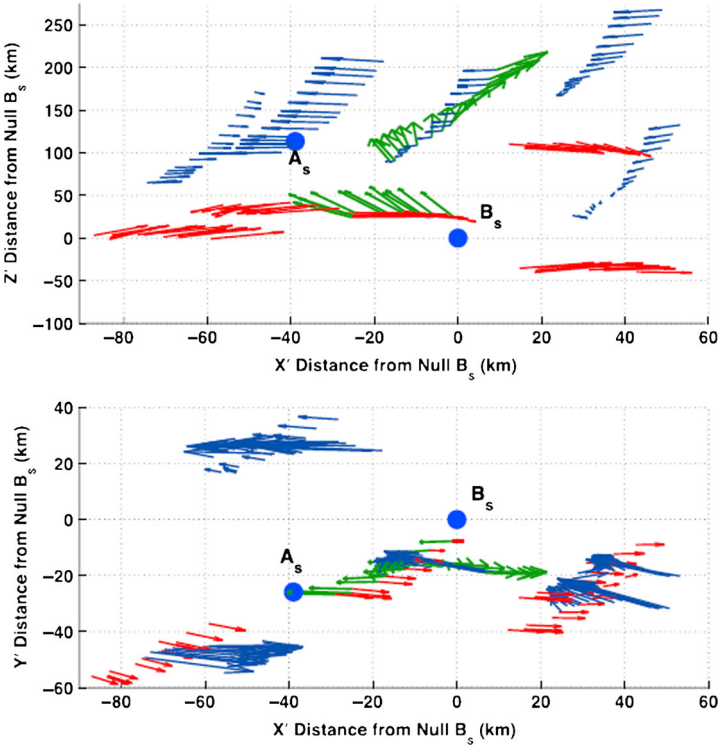

Fig. 1 Two views of a spatial map of the pair of nulls (depicted as *blue circles*) at their relative positions at the time null B_S is captured. The field lines corresponding to null A_S are shown in *dark blue*, and those belonging to null B_S in *red*. The coordinate system is the spine-aligned coordinate system of null B_S. The field lines suggest that the nulls might be topologically connected. The *green arrows* signify the curlometer current at the position of the centroid (from Wendel and Adrian 2013)

3.2 Using Three-Dimensional Particle-in-Cell Simulations to Identify the Location and Rate of Reconnection

Using one time step of a 3D VPIC simulation (also see, Daughton et al. 2011) of turbulent tearing mode reconnection, Wendel et al. (2013) investigated the location and rate of reconnection. The simulation domain encompassed roughly one to two hundred ion skin depths on a side with a resolution of roughly 0.34 electron skin depths, a guide field and open boundary conditions. The simulation's guide field geometry inhibited the formation of topological features such as separators and null points, which presented a challenge to identifying the reconnection sites, especially in the presence of turbulence. The study first determined the location of the quasi-separatrix reconnection layer predicted to occur if there is also a parallel electric field (Priest and Démoulin 1995; Titov et al. 2002). Wendel et al. produced a 2D map of the quasi-potential as a function of the Euler coordinates at the starting y-plane of the integration by integrating the parallel electric field along field lines. The quasi-potential theory of general magnetic reconnection predicts that reconnection occurs on those field lines that have a spatial gradient with respect to the Euler coordinates, while the maximum value of the quasi-potential gives the reconnection rate (Hesse and Schindler 1988; Schindler et al. 1988;

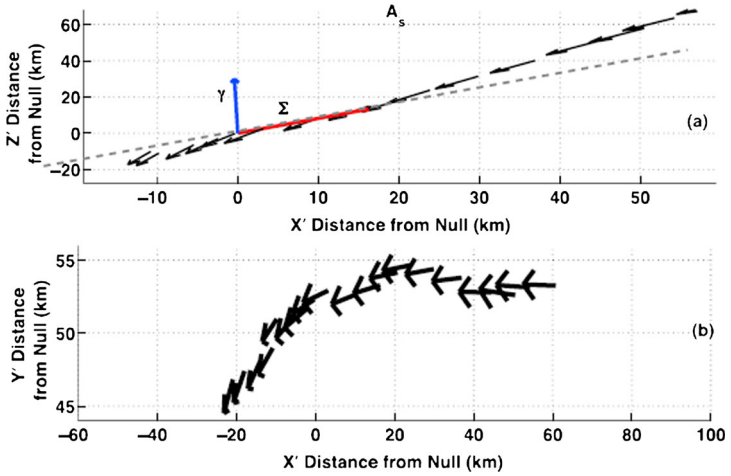

Fig. 2 (**a**) View along the normal to the plane defined by the spine and the perpendicular current of the drift flows (*black arrows*) near null A_s in the null rest frame. The data are from Cluster 1 and lie at the position of Cluster 1. The *blue* and *red arrows* are the spine and fan plane, respectively. The spine and fan directions are determined at the position of the centroid at closest approach to the null but are here placed at the null. The *dashed gray line* is an extrapolation of the fan plane. (**b**) View of the same flows along the direction of the spine. The flows can be seen to rotate around the spine (from Wendel and Adrian 2013)

Hesse et al. 2005). Hesse and Schindler (1988) showed that a necessary and sufficient condition for reconnection is

$$\nabla_{a,b}\Xi(\alpha,\beta) \neq 0$$

where Ξ is the integral of the parallel electric field along a field line and α and β are the Euler potentials. They further showed that the Hamiltonian form of the time evolution of the Euler variables produces changes of Ξ in α–β space, and therefore new field line connections in closed loops. Hesse et al. (2005) demonstrated that the rate at which flux was reconnected across an entire flux surface was given by $\max(\int E_{||}) = -\max(\Xi)$, i.e. the maximum value along the surface. This approach smoothed over the large amplitude fluctuations in the parallel electric field and revealed the parallel major contributions to the reconnection rate.

From a topological point of view, when a volume of field lines rapidly passes through a non-ideal region, magnetic connections can change. This process first requires that there be a region of large but continuous gradients in the footpoint mapping. A quasi-separatrix layer, or QSL, is such a layer of field lines whose footpoints are neighbors at one end but map to widely separated locations at the other end. The degree of flipping of magnetic footpoints is measured by the squashing factor Q (e.g., Titov et al. 2002). A value of Q that exceeds a certain threshold (a conservative estimate is at least ten times the average value over the volume (Priest and Démoulin 1995)) indicates the footpoints of a QSL. If the QSL also supports a parallel electric field, then reconnection occurs for sufficient footpoint motion. In this case, the field line velocity exceeds the local plasma velocity, producing a parallel electric field (Priest and Démoulin 1995; Titov et al. 2002). Figure 3 shows the QSL derived by integrating field lines through half of the VPIC simulation domain along the current direction. The QSL is blue, while the footpoints at the start of the integration are pink.

The QSL strongly correlates with the boundaries of the region of field lines that have a pronounced quasi-potential. The QSL carrying a parallel electric field therefore satisfies the

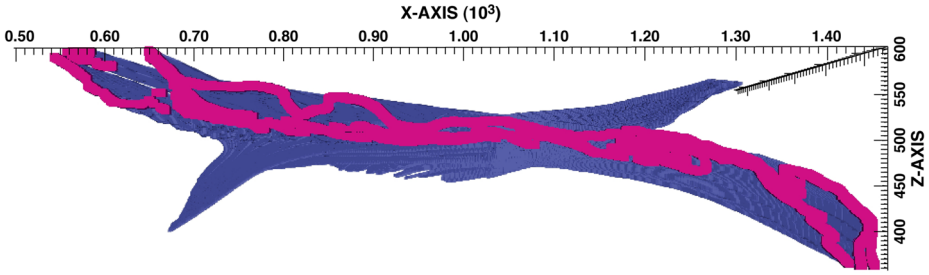

Fig. 3 The hyperbolic structure of the QSL between $y = 100$ and $y = 1024$ grid points based on $Q \geq 10^4$ in the VPIC simulation. The *blue surface* is the QSL, which twists from one orientation to another along y, and the *pink layer* corresponds to the endpoints of the QSL at the start plane at $y = 100$ (from Wendel and Adrian 2013)

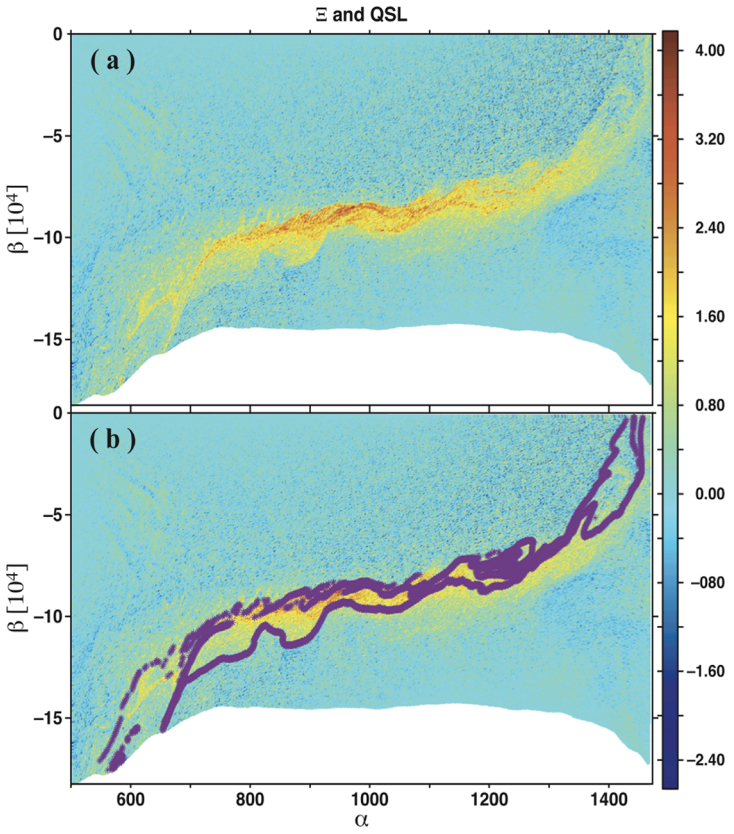

Fig. 4 (**a**) A map of Ξ in terms of the Euler variables $\alpha = x$ and $\beta = -\int B_y(x, z')\mathrm{d}z'$. (**b**) The map of Ξ overlaid with the footpoints of the $Q \geq 10^4$ QSL, shown in *purple*. Here Ξ is in units of $v_A B_0 d_i/c$ (from Wendel and Adrian 2013)

general necessary and sufficient condition for 3D magnetic reconnection, viz., that in the absence of null points there must be a gradient of the quasi-potential, or integrated parallel

electric field, with respect to the Euler variables. The prediction that reconnection occurs in loop-like structures also agrees with the elongated, but generally loop-like shape of the gradients of Ξ and of the QSL. The turbulence produces finer structure within the loop. The maximum Ξ gives a normalized reconnection rate across the QSL of about $0.1 v_A B_0/c$, where v_A is the Alfvén speed, B_0 is the background reconnecting magnetic field, and c is the speed of light. Figure 4a is a map of Ξ in the starting plane of the integration as a function of the Euler variables α and β, while Fig. 4b is the same map with the footpoints of the QSL as a function of α and β superimposed in purple (Ξ is in units of $v_A B_0 d_i/c$, where d_i is the ion skin depth).

To further illustrate how and where $E_{||}$ was distributed along the QSL field lines that did support reconnection, the running sum of the parallel electric field along the field lines was followed. The field lines that are reconnecting carry a relatively steady DC contribution to the reconnection rate that is absent on field lines that are not reconnecting, although both types of field lines have fluctuating positive and negative values of the parallel electric field. The reconnection rate resulted entirely from the DC and linear trends in $E_{||}$. Reconnection occurred along a field line wherever the running sum of $E_{||}$ was increasing.

The ramifications for the interpretation of reconnection in three-dimensional turbulence both in simulations and in observations is that the location and rate of reconnection is governed by low-order coherent structures even when fields are highly stochastic and currents are filamented. While it is certainly possible that both fluctuations and double layers contribute to the physics that sustains the average reconnection electric field, it is the average DC field that governs the reconnection rate. The results also affect the inferred location of the site of reconnection and the rate of reconnection as determined from observations. *If the medium is not laminar, as is usually the case in the magnetosheath and plasma sheet, then the reconnection rate cannot be inferred from a local parallel electric field measurement, but rather must be estimated from the spatial average along a field line, or by some other means*.

4 The Nightside: Studies of Reconnection in the Magnetotail

4.1 Studies of the Electron and Ion Diffusion Regions

The multi-scale nature of reconnection has long been a focus of study in both space and laboratory plasmas. The initiation and reconfiguration of magnetic topology associated with reconnection are thought to arise as a result of demagnetization of electrons within the small electron diffusion region (EDR) that is embedded within the much larger ion diffusion region (IDR) where ions are demagnetized. IDRs, where Hall physics governs the magnetofluid description, have been identified by their magnetic and electric field geometry (see, e.g., Wygant et al. 2005; Vaivads et al. 2006; Eastwood et al. 2010a, 2010b).

The EDR is difficult to identify in data from current spacecraft (but see Scudder et al. 2012), but current measurements can delineate the substructure of the current sheet where reconnection is occurring. Chen et al. (2008) and Wang et al. (2010) used the observations of temperature anisotropy and variations in electron moments to identify magnetic islands and the scale sizes of an electron current layer. The anisotropic electron pressure with $p_{||} > p_{\perp}$ within the reconnection region was first reported by Øieroset et al. (2002) and the divergence of the electron pressure tensor was first measured using the four Cluster spacecraft by Henderson et al. (2008). The anisotropy was accounted for in a numerical study by Egedal et al. (2005), who found that it caused electron trapping by magnetic mirror forces and parallel

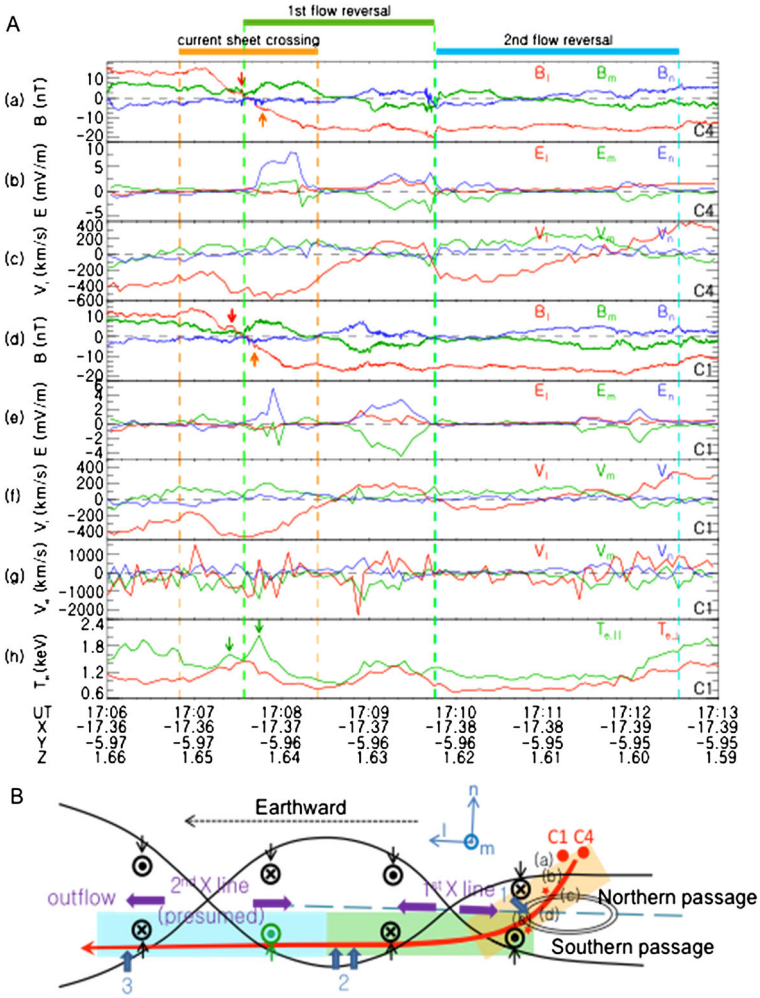

Fig. 5 **A**. C4 (a–c) and C1 (d–h) data in the current-sheet coordinates: (a, d) magnetic field, B_l (*red*), B_m (*green*), and B_n (*blue*); (b, e) electric field, E_l (red), E_m (*green*), and E_n (*blue*); ion (c, f) and electron (g) velocity, V_l (*red*), and V_m (*green*), V_n (*blue*); (h) electron parallel (*green*) and perpendicular (*red*) temperature. **B**. The relative trajectory of C1/4 across the multiple X-line structures. *Orange*, *green*, and *blue shades* depict the current sheet crossing, the first, and the second flow reversal, respectively. *Red stars* (*bottom panel*) indicate a possible northern and southern traversal of the plasmoid structure embedded in the outflow region, associated with a transient enhancement of B_l, marked by *red* and *orange arrows* in panel **A**(a, d) and electron temperature anisotropy ($T_{||} > T_{\perp}$, *green arrows* in panel **A**(d)). During the second flow reversal (*blue-shaded region*), C1 did not observe tailward-side Hall fields (denoted by *green symbols*), although such fields were observed by C4 later. (From Hwang et al. 2013)

electric fields. Egedal et al. (2008) derived an analytical form of the electron distribution function that accounted for the anisotropy. Egedal et al. (2010) compared the analytic result to the anisotropic electron distributions observed by Cluster in the October 1, 2001 event (Chen et al. 2008). Lê et al. (2009) derived new fluid-closure equations to describe the state functions ($p_{||}$ and $p_{\perp}$) for magnetized electrons in a collisionless regime in which electron trapping accurately treated the pressure anisotropy. In subsequent fluid simulations using the

new fluid closure relationships, Ohia et al. (2012) demonstrated that the pressure anisotropy could drive large-scale elongated electron current layers within the reconnection region.

4.2 Multiple X-line Structures Observed by Cluster

Hwang et al. (2013) used magnetic field and thermal electron and ion measurements from Cluster in the vicinity of a reconnection X-line to delineate the structure of the reconnection current sheet (Fig. 5). Multi-point Cluster observations on August 18, 2002 indicated that an X-line drifted close to the spacecraft, about $3.4R_{\mathrm{E}}$ earthward of the position where another X-line had been observed earlier. This observation provided important clues about the structure of reconnection layers and how X-lines develop and evolve. Comparison of the Hall magnetic and electric field geometry and the observed properties of energetic electron beams streaming along the separatrix between the Cluster spacecraft, indicated that the second X-line formed within 20 seconds of the observation of the first one. Repeated flow reversals and the observed Hall field geometry further suggested that the initial current sheet was unstable to the tearing-mode. In particular, the presence of a magnetic island embedded in the outflow region downstream of the first X-line appeared to be coincident with an outflowing super-Alfvénic electron jet, suggesting that an instability in the elongated electron current sheet might have caused the plasmoid to form (Karimabadi et al. 2007).

Figure 6, shows detailed features of the electron distribution functions along the spacecraft trajectory across the current sheet (Hwang et al. 2013). In particular, Hwang et al. reported that near a reconnection X-line there was a unique signature in the electron distribution function associated with traversing a sharp boundary in the electron current sheet. They identified a region with a thickness of 0.72 ion inertial lengths (29 electron inertial lengths, d_e) of super-Alfvénic electron outflow (greater than the ion in-flow Alfvén speed) during the period when the spacecraft were in the vicinity of the neutral sheet. Slightly below the neutral sheet, asymmetric counter-streaming electrons were observed that lacked axisymmetry in the electron ($V_{\perp 1}$, $V_{\perp 2}$) distribution functions over a thin boundary with a thickness of several d_e. This electron-scale transition layer was embedded in a much wider region where both the ion and electron Walén test failed and where electron super-Alfvénic bulk outflow jets were detected. Those phenomena illustrate details of the substructure of the reconnection current sheet and suggest that the spacecraft traversed or skimmed the tailward edge of an elongated electron current layer.

4.3 Dipolarization Fronts and Their Relationship to Reconnection in the Magnetotail

Dipolarization fronts (DFs) are a phenomenon commonly detected near the equatorial plane of the Earth's tail plasma sheet. Rapid ($\ll 1$ minute) increases in the north- to south-directed component of the magnetic field (B_{Z}) have been reported in the near-Earth plasmasheet during magnetospheric substorms (Russell and McPherron 1973; Angelopoulos et al. 1992; Runov et al. 2009b, 2011). They are generally found near the leading edge of the rapid earthward flows (hundreds of km/s) called bursty bulk flows (BBFs) (Baumjohann et al. 1990; Angelopoulos et al. 1992). THEMIS data showed that the dipolarization fronts generally propagate earthward from at least the near-Earth tail. A rapid increase of B_{Z} is preceded by a decrease of smaller amplitude (Ohtani et al. 2004). The front is generally followed by a decrease in both the thermal plasma density and temperature (Wolf et al. 2009, and references therein). Earthward propagating dipolarization fronts and BBFs may be responsible for most of the earthward transport of energy and magnetic flux from the magnetotail to the inner magnetosphere (Angelopoulos et al. 1994).

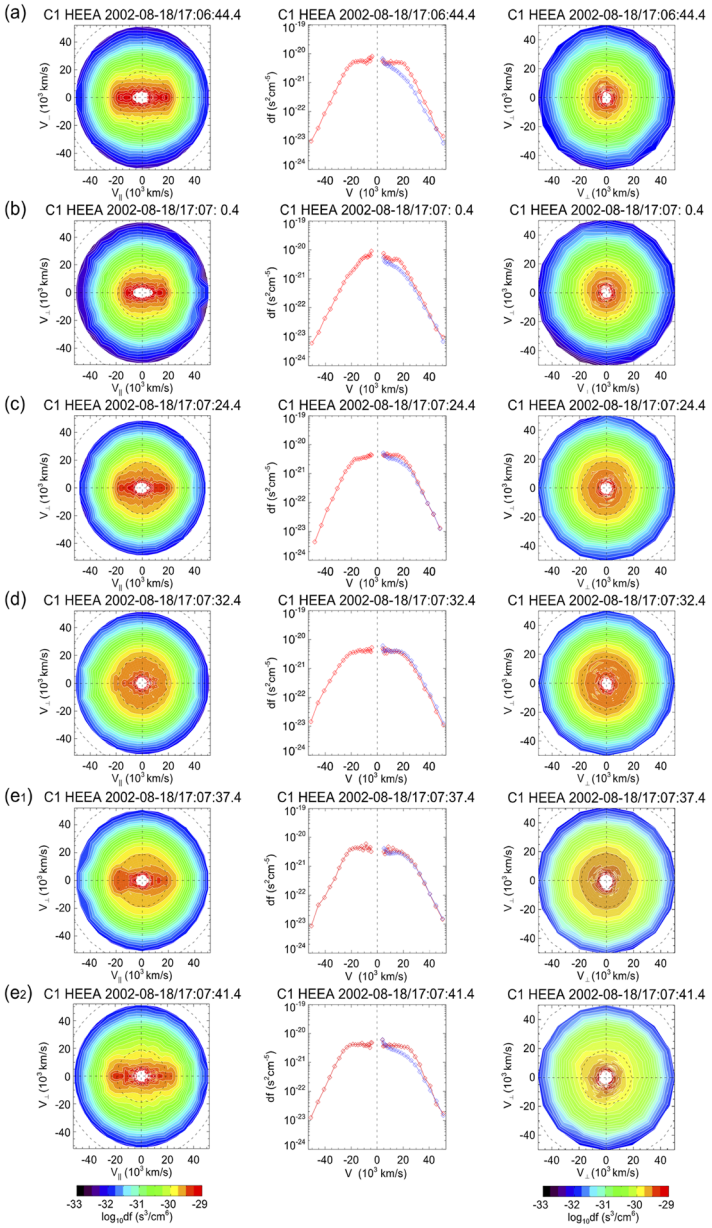

Fig. 6 The electron distribution functions at the time of crossing the inflow region at ∼ 1706:44 UT (**a**), a separatrix at ∼ 1707:00 UT (**b**), the northern-hemispheric boundary of a magnetic island downstream of the X-line at ∼ 1707:24 UT (**c**), the neutral sheet with a minimum of magnetic strength at ∼ 1707:32 UT (**d**), and slightly below the neutral sheet at ∼ 1707:40 UT (e1 and e2). The *first column* shows the electron distributions as a function of ($V_{||}$, $V_{\perp}$), the *middle* one shows the reduced distribution functions along the direction parallel (*red*) and perpendicular (*blue*) to the local magnetic field, and the *last* one shows the distributions as a function of ($V_{\perp 1}$, $V_{\perp 2}$) from the 3-D electron distributions. Corresponding locations where in the current sheet frame the electron distributions are sampled are denoted along the spacecraft trajectory in Fig. 7B(a–e). Inner (outer) *dashed circles* overlaid in all 2-D distribution plots correspond to velocities of electron energies of 1 (10) keV. (From Hwang et al. 2013)

Data from Cluster showing numerous DF observations at the near-Earth plasma sheet (Nakamura et al. 2002; Fu et al. 2011, 2012; Hwang et al. 2011a, 2013; Schmid et al. 2011) and THEMIS (Runov et al. 2009b; Sergeev et al. 2009; Deng et al. 2010a, 2010b, Dubyagin et al. 2010; Zhou et al. 2010; Ashour-Abdalla et al. 2011; Runov et al. 2011) also indicate that DFs predominantly propagate earthward along the radial direction and are often embedded within fast earthward flows. Figure 7 shows a series of six dipolarization fronts observed by Cluster (Hwang et al. 2011a). They are numbered at the top of Fig. 7 and by magenta vertical lines. These DFs have a typical duration of 2–4 seconds and a thickness of 900–1500 km, which is comparable to the inertial length or gyroradius of H^+ ions. Earthward BBFs follow 1.5–2 minutes after a DF passage for DFs 1–3, and 5 (Fig. 7m), which is, however, not clear for DF 4 and not shown for DF 6, which propagates tailward. The velocity of the fast earthward flow following behind DFs 1–3 is comparable to the Alfvén velocity, indicating that the flow bursts might have been generated by bursty reconnection that occurred tailward of the spacecraft.

Common features across each DF are a sharp jump in B_z (Fig. 7a), a drop in the plasma density (Fig. 7b), a corresponding decrease in plasma β (Fig. 7i), a decrease in the plasma pressure and an increase in the magnetic pressure (Fig. 7j). These variations across the DFs indicate that DFs carry an entropy-depleted flux tube, or localized "plasma bubble" behind the DFs. Panel Fig. 7k demonstrates a decrease in the entropy, calculated from the ion distribution function (black in Fig. 5k), or the flux-tube entropy parameter (using Wolf et al. 2006's formula, red in panel Fig. 11k).

Traditionally, dipolarization of stretched tail magnetic field, which is often accompanied by observation of a DF, is believed to be associated with a decrease of the cross-tail current in the near-Earth region that might be caused by a cross-tail current instability (Lui et al. 2006). More recently, DFs are also thought to result from magnetic reconnection in which the exhaust jets and entrained magnetic fluxes from the reconnection region pile up, forming a front of increased current-sheet-normal magnetic field (Hoshino et al. 2001; Hoshino 2005; Nakamura et al. 2009; Sitnov et al. 2009). In kinetic simulations, Sitnov et al. (2009) showed that DFs can form as a result of transient reconnection.

Hwang et al. (2011b) concluded from the example in Fig. 7 that multiple DFs can result either from bursty reconnection events or from continuous reconnection in which the rate fluctuates on the time scale of about 3 minutes, corresponding to the occurrence rate of multiple DFs. They noted that the density ratio of O^+ to H^+ ions increased from $\sim$5% before the first DF to $\sim$20% at the end of the event, indicating that a series of bursty reconnection events evolved from the plasma sheet to the lobe and that the repeated reconnection events might have triggered formation of multiple DFs, which could have arisen from patchy reconnection. Recent studies by Liang et al. (2014), using a global MHD simulation of this event showed numerous simultaneous reconnection sites dispersed over the near Earth current sheet.

4.4 Reconnection, Dipolarization Fronts and Particle Acceleration

The most commonly posited cause for dipolarization fronts, BBFs and depleted flux tubes, is sporadic and spatial localized reconnection (Sergeev et al. 1992, and other references). Dipolarization fronts generated by reconnection have been found in both quasi-local and global MHD simulations (Wiltberger et al. 2000; Birn et al. 2004; Ashour-Abdalla et al. 2011; Birn et al. 2011), hybrid simulations (Krauss-Varban and Karimabadi 2003) and two-dimensional particle-in-cell kinetic simulations (Sitnov et al. 2009; Sitnov and Swisdak 2011). However, other mechanisms, including the ballooning interchange instability (Hurricane et al. 1996;

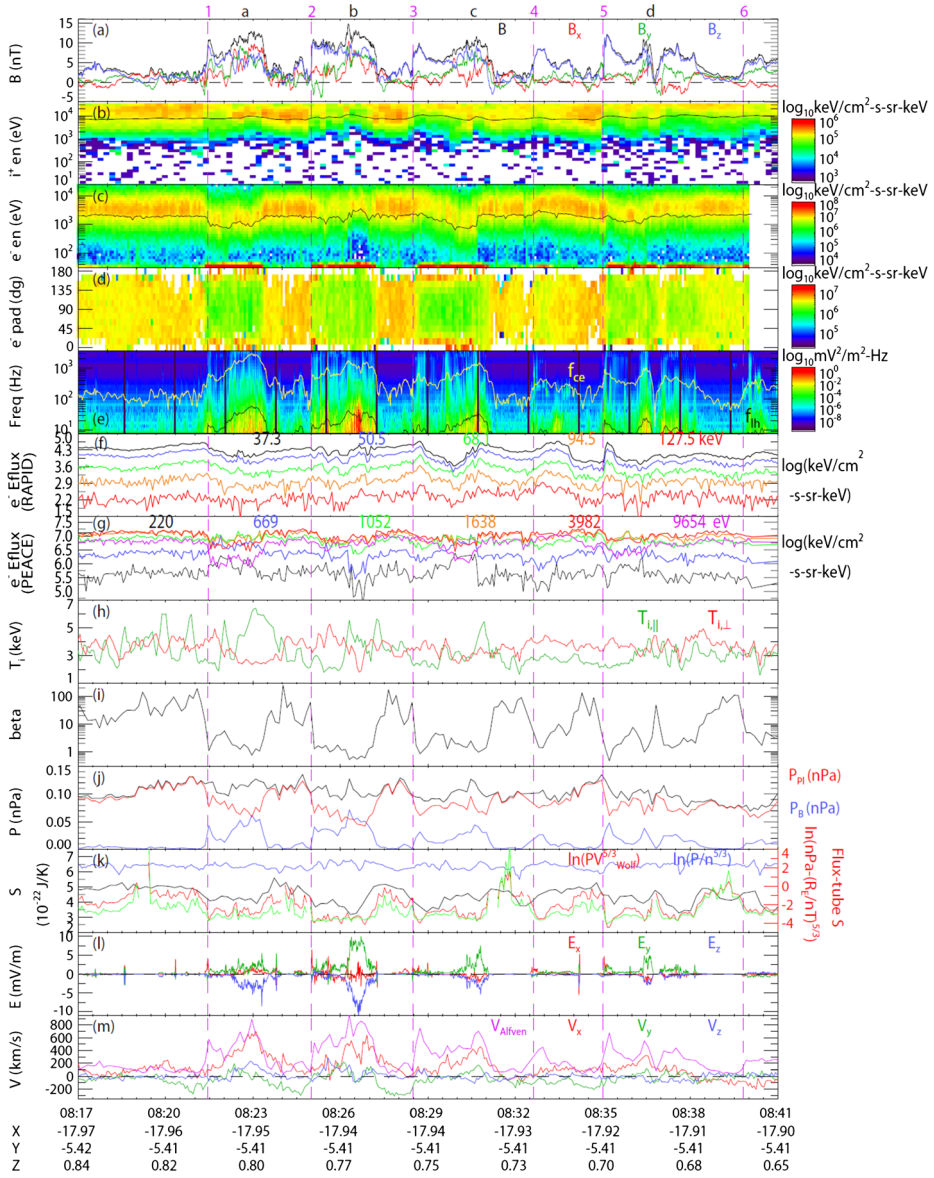

Fig. 7 The field and plasma signatures of the event reported by Hwang et al. (2011a). (**a**) The magnetic field, $|\mathbf{B}|$, B_x, B_y, and B_z; (**b**, **c**) the energy spectrogram of ions and electrons (the characteristic energy, defined as the energy flux divided by the number flux is overplotted in *black*); (**d**) the electron pitch angle distribution; (**e**) the wave spectral power densities from the electric field (lower-hybrid frequency, f_{lh} and electron cyclotron frequency, f_{ce} are denoted as *black* and *yellow curves*); (**f**, **g**) the electron energy fluxes; (**h**) the ion parallel (*green*) and perpendicular (*red*) temperatures; (**i**) the plasma β; (**j**) the plasma (*red*) and magnetic (*blue*) pressures, and the sum of the two (*black*); (**k**) the entropy calculated from the ion distribution function (*black*), the entropy parameter or "flux-tube entropy" (*red*) defined by PV_B^{γ}, derived using the Wolf et al. (2006) formula for the estimation of the volume of a closed flux tube, V_B (the *green curve* shows one third of the estimated V_B), and the specific flux-tube entropy using the ion density, $P/n^{5/3}$ (*blue*); (**l**) the electric field, (**m**) the ion velocity (the local Alfvén velocity is shown in *magenta*). Parameters are shown in GSM coordinates (from Hwang et al. 2011a)

Pritchett and Coroniti 2010; Lyatsky and Goldstein 2013), may also be important for forming dipolarization fronts and for determining their azimuthal extent.

At the passage of DFs. the thermal plasma density decreases, fluxes of energetic ions and electrons increase dramatically to hundreds of keV (Runov et al. 2009a, 2009b, 2011; Sergeev et al. 2009; Ashour-Abdalla et al. 2011; Hwang et al. 2011a). But exactly how and where these energetic electrons are accelerated is not well understood. Work to date has concentrated on two areas: acceleration at or near the reconnection region and acceleration as the particles propagate earthward. There are many recent reviews that have summarized our present understanding (see, e.g., Birn and Priest 2007). An important result is that when kinetic effects are included, reconnection progresses at a faster pace than it does in MHD and there are two regions associated with the reconnection process that are the sites of intense energy exchange: separatrix regions and electron jets.

The regions around the separatrices (the separatrices are the boundary between open and closed field lines associated with x-points in 2D and, as pointed out above, magnetic surfaces in 3D) in kinetic reconnection generate intense electron flows that lead to a variety of waves and instabilities. At scales approaching the ion Larmor radius, localized electric fields with Hall physics signatures appear. These fields extend a great distance away from the reconnection x-point, transferring sizeable amounts of energy (Shay et al. 2011). The Hall electric field has a significant electrostatic component due to the local breakdown of charge neutrality (Huang et al. 2006). In addition, the differences in the electron and ion speeds lead to localized (on the electron skin depth scale) electron jets that emerge from the reconnection region (Fujimoto 2006; Karimabadi et al. 2007). Both the Hall region along the separatrices and the electron jets extend for long distances (Phan et al. 2011; Shay et al. 2011), carrying significant amounts of energy. The separatrices are characterized by strong perpendicular and parallel electric fields that lead to strong electron energization (Egedal et al. 2012).

Separatrix regions and electron jets are both sensitive to the specific conditions of the reconnecting plasma. At the separatrices, the Hall physics and the formation of electron cavities (regions of depleted electron density) are affected in strength by the presence of a guide field (Lapenta et al. 2010, 2011), which, although typically weak in the magnetotail, nevertheless can have amplitudes of up to 20% of the reconnecting field. The electron jets emerging from the reconnection region also are affected by those guide fields (Goldman et al. 2011), leading to the possibility that typical magnetotail values of the guide field can either suppress or enable the electron jets (Lê et al. 2013).

An additional, or alternative, location for acceleration of particles is the magnetic pile-up region formed as dipolarization fronts impinge on the inner magnetosphere (Kivelson 1980; Birn et al. 2004; Asano et al. 2010; Birn et al. 2011). Kinetic simulations (Sitnov et al. 2009) showed that electrons do not necessarily need to be energized at the x-line and that energy dissipation is stronger at the dipolarization front than it is at the initial reconnection region. Strong electron energization at dipolarization fronts has been well established by observations in the magnetotail (Runov et al. 2009a, 2009b; Sitnov et al. 2009; Zhou et al. 2009).

Figure 8 shows an example of the relationship between decreases in the thermal electron fluxes and increases in the energetic electron fluxes during passage of a dipolarization front. The energy flux for channels between 30 keV and 207 keV (third second panel) show a marked increase coincident with the dipolarization front, while the lower thermal energy plasma measured by ESA (< 30 keV) (fourth third panel) shows a simultaneous decrease. Fluxes at the two highest energy channels, 297 keV and 421 keV, do not show any noticeable

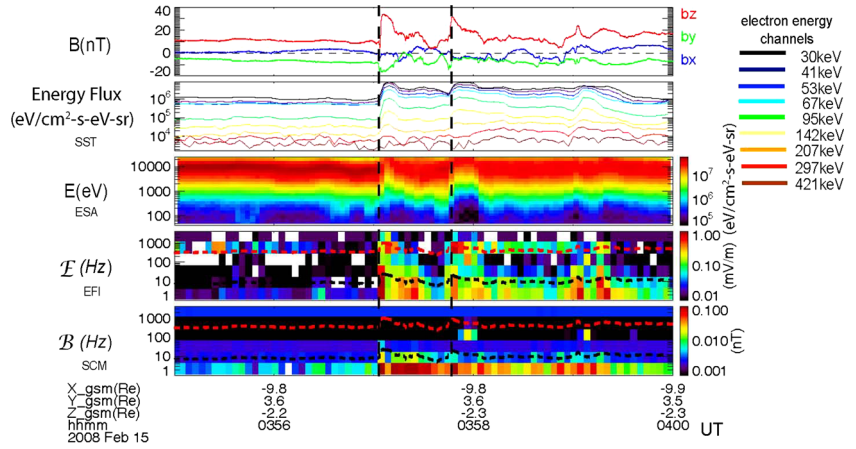

Fig. 8 Observations from THEMIS P4 on February 15, 2008. The three curves in the *top panel* contain the three components of the magnetic field in GSM coordinates. The *second panel* gives energy fluxes of energetic electrons from the SST instrument with the energy scale on the *right*. A spectrogram of the energy flux from the ESA instrument is in the *third panel* while dynamic spectra of the electric and magnetic field waves are in the *last two panels*. The *dashed lines* give the lower hybrid (*black*) and electron cyclotron frequencies (*red*). (From Ashour-Abdalla et al. 2011)

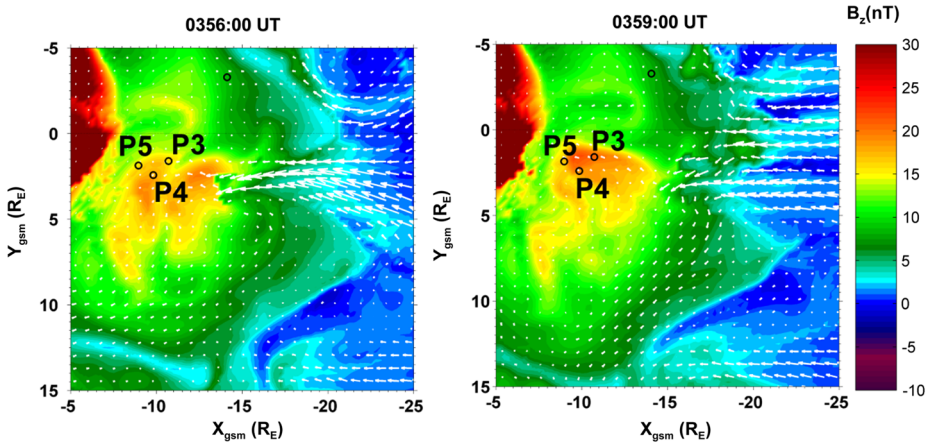

Fig. 9 Color spectrogram giving the B_Z component of the simulated magnetic field on the maximum pressure surface. The *white arrows* show the flow vectors. The *left plot* was made at 0356UT and the *right plot* at 0359UT. (From Ashour-Abdalla et al. 2011)

change, indicating that the upper limit for energization is ~ 200 keV. At the time of the dipolarization there was a coincident increase in both electric and magnetic field amplitudes. Electric field wave amplitudes were enhanced from below $f_{\rm lh}$ to above $f_{\rm ce}$. The magnetic field wave amplitudes were concentrated below $f_{\rm lh}$ except at 03:58 UT and 03:59:10 UT when electromagnetic whistler waves were observed. This increase in energetic electron flux is occurring several $R_{\rm E}$ away from the reconnection site, which suggests that acceleration is not confined to the neutral line (Zhou et al. 2009; Asano et al. 2010; Ashour-Abdalla et al. 2011).

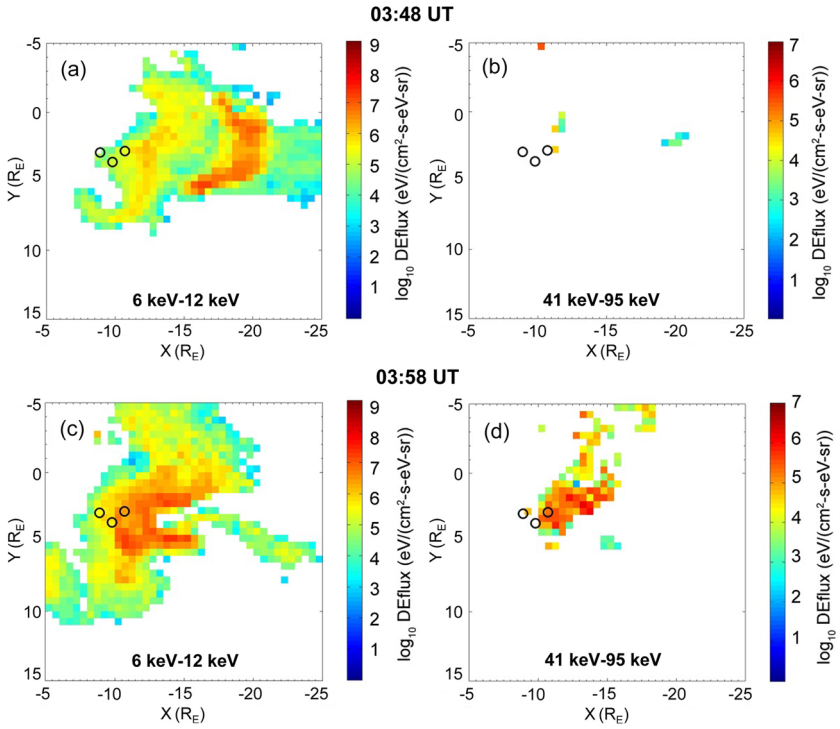

Fig. 10 Plots of differential energy flux on the maximum pressure surface in a global MHD simulation for two different energy channels. Panels (**a**) and (**b**) are at 3:48 UT and panels (**c**) and (**d**) are at 3:58 UT. (From Ashour-Abdalla et al. 2011)

Figure 9 shows results from an MHD simulation of this substorm. Two dipolarization fronts can be seen as enhancements of the B_z component on the surface of maximum thermal pressure (yellow and orange shading) at 0356 UT and 0359 UT centered near $X_{gsm} = -9R_E$ and $-12R_E$ and $Y_{gsm} = 2.4R_E$. The first front was first seen at P4 and then at P5. The MHD results suggest that the first front for the most part missed P3. However, the second front was observed by all three THEMIS spacecraft starting at 0359 UT, first at P3, then at P4 and finally at P5.

Using the electric and magnetic fields from this MHD simulation, electrons were launched from a region in the magnetotail around $X_{gsm} = -20R_E$ downtail and $0 < Y_{gsm} < 5R_E$ on the dusk side and their trajectories were followed by using a combination of full particle and guiding center calculations (e.g., Schriver et al. 1998, 2005; Ashour-Abdalla et al. 2011). This source region was determined by using the observed electron distributions and following them backwards in time to identify where they originated. The κ parameter, which in this section is a measure of adiabaticity and is defined as the square root of the local magnetic field radius of curvature divided by the local Larmor radius (Büchner and Zeleny 1986, 1989), was used to determine whether it was necessary to calculate full particle dynamics. A large number of electrons were followed and data was collected at virtual detectors placed throughout the system (Ashour-Abdalla et al. 1993), including the locations of the THEMIS spacecraft. In Fig. 10, we show the simulated energy flux on the surface of maximum thermal pressure at two times (03:48UT and 03:58UT) and in two separate energy ranges (6–12 keV and 41–95 keV). This surface is a good proxy for the center of the

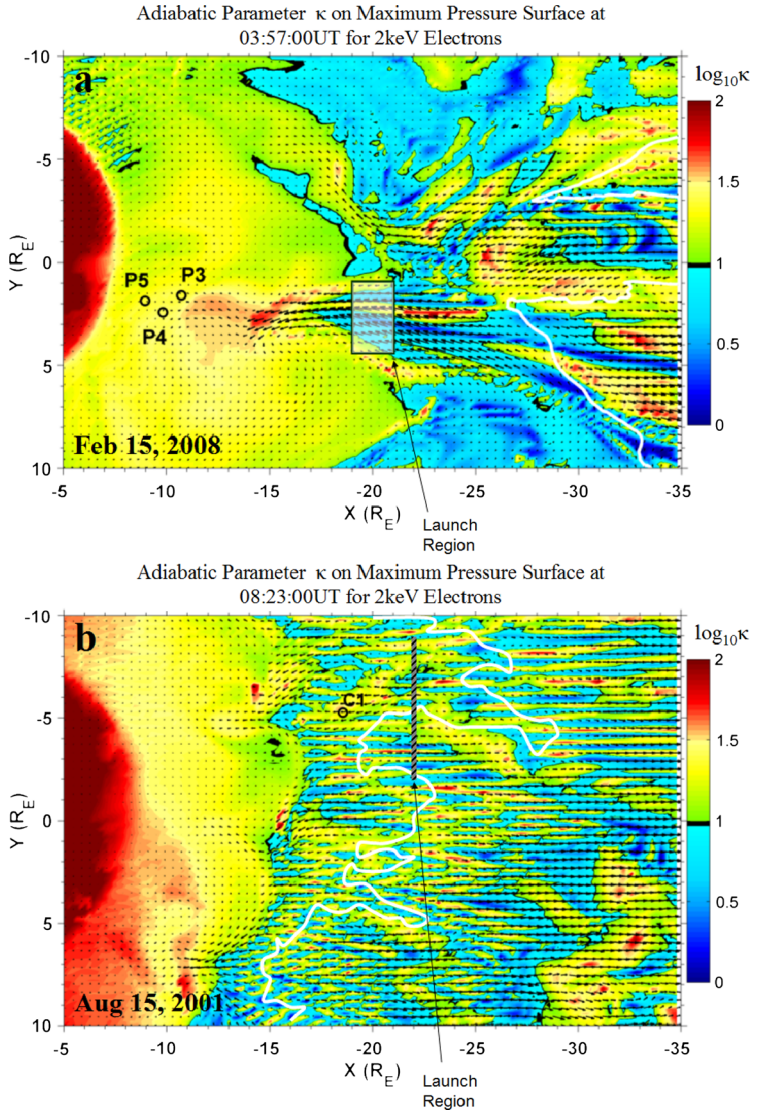

Fig. 11 Adiabatic parameter κ on the surface of maximum pressure for February 15, 2008 (**a**) and August 15, 2001 (**b**). *White solid line* represents the neutral line. Flow vectors are given by *black arrows* (from Liang et al. 2014)

current sheet (Ashour-Abdalla et al. 1999, 2002). At 03:48UT there are few high-energy particles present anywhere. The largest fluxes of electrons in the 6–12 keV range are near the neutral line, which remained near $x \sim -19R_E$ at both times. At 03:58UT, both low energy particles and high-energy particles are visible and both populations are concentrated near the inner boundary of the dipolarization front (between $x \sim -11$ and $-15R_E$). Thus, the Large Scale Kinetic (LSK) calculations indicate that, while low energy electrons appear rapidly in the vicinity of the X-line (Fig. 10a), high energy particles are present only after the dipolarization front has moved inward (Fig. 10d). Low energy particles appear

to be convected with the dipolarization front and provide a seed population that is energized in the rapidly changing magnetic field of the inward-moving dipolarization front. The strongest enhancements in energy flux actually occur several R_E away from the reconnection region.

The observations of dipolarization fronts can differ significantly (Ashour-Abdalla et al. 2011; Hwang et al. 2011a). For example the magnetic field increases associated with the dipolarization fronts on August 15, 2001 (Cluster; 5–10 nT in Fig. 7) are much smaller than those on February 15, 2008 (THEMIS; 30 nT in Fig. 8). The energetic electrons decrease at some of the dipolarization fronts in Fig. 7, while they increase at all three in Fig. 8 (see Table 1 in Liang et al. 2014 for a list of differences). Liang et al. (2014) have investigated possible causes for those differences. They used the same LSK approach that was used for the February 15, 2008 substorm to model the August 15, 2001 substorm and investigated the acceleration mechanism for both events. The MHD simulations showed that very different magnetotail configurations formed these events, which had contrasting flows, magnetic reconnection configuration, and plasma sheet structure. For February 15, 2008, the reconnection is localized within a narrow region of high-speed flow. In contrast, for the August 15, 2001 event there is a wide neutral line extending across the tail with low-speed flows. These differences lead to contrasting occurrence rates of non-adiabatic acceleration. In Fig. 11 the adiabaticity parameter κ is plotted in the maximum pressure plane. The electrons are non-adiabatic (blue shading in Fig. 11) over much of the tail on August 15, 2001 while for February 15, 2008 the region of non-adiabaticity is narrow. On February 15, 2008 the electrons move through the non-adiabatic region quickly with fast earthward flows ($\sim$ 300 km/s) and then experience adiabatic acceleration. On August 15, 2001 they remain in the non-adiabatic region for much longer due to the relatively slow earthward flows ($\sim$ 100 km/s). *Therefore, increased energetic electron fluxes are not necessarily a signature of nearby reconnection or acceleration occurring at the neutral line*. Liang et al. (2014) then addressed why the two substorms had such different magnetospheric configurations even though the solar wind conditions for the two events were reasonably similar with dominant IMF B_y. They found that on February 15, 2008 dayside reconnection occurred near the subsolar point due to a large (23°) tailward dipole tilt, while on August 15, 2001 it occurred on the flanks of the magnetopause leading to very different magnetospheric configurations.

For the February 15, 2008 substorm the observations by THEMIS were near the dipolarization front ($x \sim -10R_E$), and for the August 15, 2001 substorm the observations were near the reconnection site ($X \sim -17R_E$). Pan et al. (2014) examined another event on March 11, 2008, that was observed by THEMIS spacecraft P3 and P4 from near the dipolarization front (P4, $x \sim -10R_E$) and by THEMIS P2 nearer the putative location of the neutral line ($x \sim -15R_E$). These multi-point measurements not only put rather strict constraints on the global MHD and LSK simulations, but also enabled them to quantify the electron energization in different regions.

In Fig. 12, Pan et al. (2014) compared the computed energy flux from their MHD/LSK calculations with THEMIS P2 observations. The top panel contains the observed energy flux for different energy channels while panel Fig. 12b shows the results from their calculations using a Maxwellian for the initial distribution function at a location near the neutral line in the MHD simulation. Clearly, the low energy channels (2–6 keV and 6–12 keV) are better represented than the higher energy channels. In fact, the calculations in that study do not reproduce any particles in the highest energy channel (41–95 keV). When they assumed that the source was distributed near the neutral line and was a combination of a 1 keV Maxwellian, together with a power law distribution based on observations by Øieroset et al.

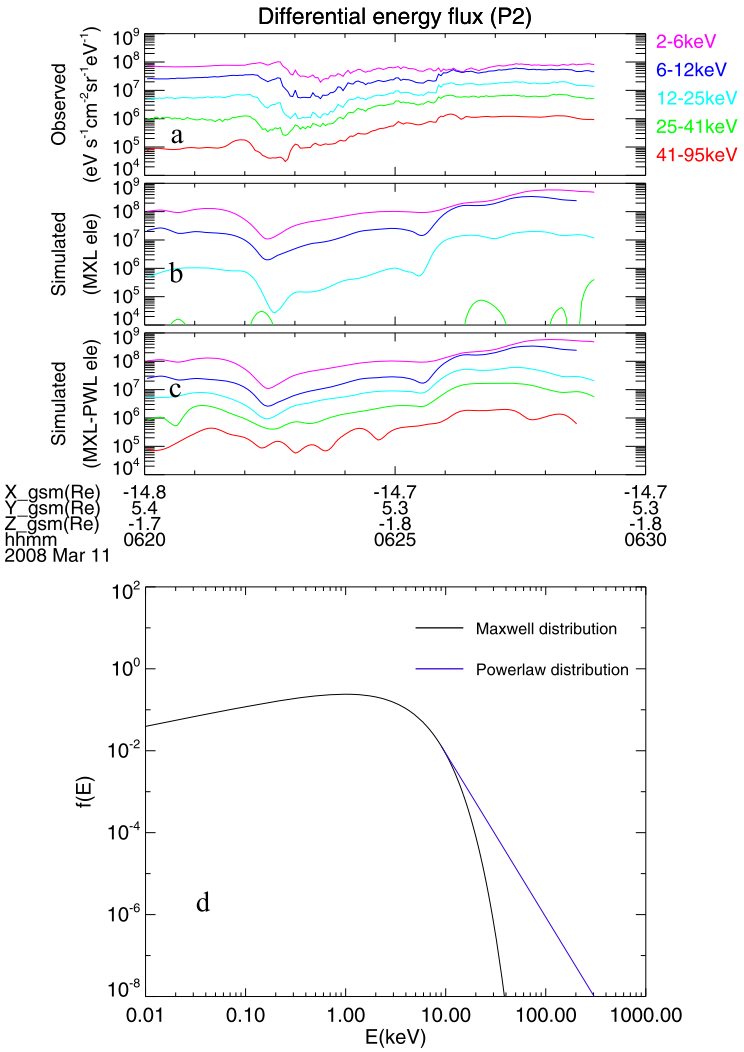

Fig. 12 The differential energy flux for THEMIS P2. Energy ranges of 5 channels are covered by both the ESA and SST instruments. Panel (**a**) shows THEMIS P2 observations, the second panel (**b**) gives the simulated energy flux using only the Maxwellian thermal electron distribution as the source, and the panel (**c**) gives the result including both the Maxwellian thermal electrons and high energy electrons (from Pan et al. 2014). Panel (**d**) shows the electron source distributions for the two LSK simulations. The first simulation includes only thermal electrons of Maxwellian distribution with 1 keV temperature (*black line*); the second simulation includes both the thermal electrons and high-energy electrons that obey a power law distribution (*blue line*) (adapted from Pan et al. 2014)

(2002) at higher energies, they got substantially better results (Fig. 12c) (Pan et al. 2014). The source distribution function near the neutral line has been plotted in Fig. 12d.

It is not surprising that the inclusion of high-energy electrons provides a better comparison between the simulations and observations since P2 is not far from the source region where the electrons were launched, and the observed electron flux at P2 has a high-energy tail. These comparisons show that the simulations need to include high-energy electrons

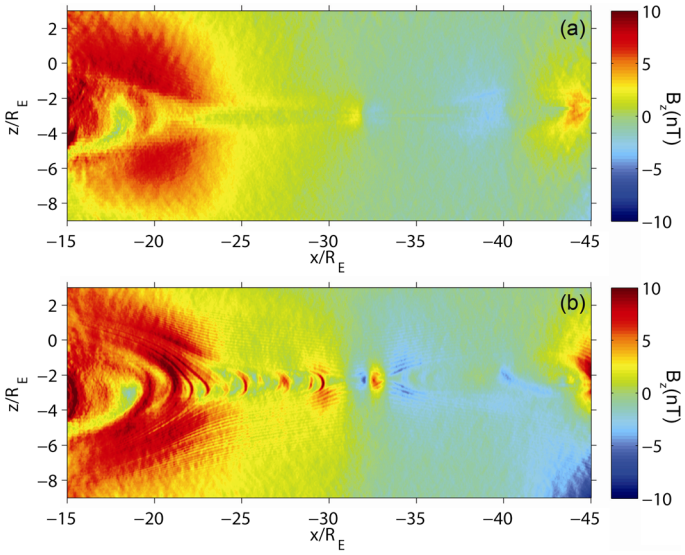

Fig. 13 The vertical magnetic field (B_Z in GSM coordinates) is shown at $t = 14.4$ s (**a**) and $t = 57$ s (**b**) (from Ashour-Abdalla et al. 2014)

with a power law distribution. The addition of the power law to the source distribution also improved the agreement at P3 and P4 nearer the Earth (Pan et al. 2014). The distribution function with the power law dependence adds a free parameter to the analysis that enhances the ability of obtaining a better fit to the observations. However, that the improvement is so dramatic, suggests strongly that for this event the physics near the neutral line is very important for understanding the electron dynamics.

4.5 Dipolarization Fronts, Reconnection and MMS

Neither the LSK simulations nor the PIC simulations give a complete picture of the physics of reconnection in the magnetotail. The LSK simulations use the electric and magnetic fields from global MHD simulation. And while the MHD simulations are self-consistent, the resistivity that allows reconnection to occur is arbitrary. In addition, the LSK particle calculations are not self-consistently tied to the MHD results. PIC simulations contain the full physics of reconnection but are very expensive to run and therefore are generally limited to idealized calculations over small spatial domains. In reality the reconnection in the magnetosphere is determined by the overall changes in the solar wind and magnetosphere interaction that occur on magnetospheric scales. In support of MMS we have developed a simulation approach in which the UCLA global MHD simulation is coupled with an implicit particle in cell simulation (Markidis et al. 2010; Ashour-Abdalla et al. 2014). The work is motivated by the solar physics work of Baumann et al. (2013). In the first study, the new system was used to model the February 15, 2008 substorm discussed above. A two-dimensional version of the iPIC3D code (modeling the XZ plane) was run in the magnetic field and plasma configuration from the MHD code just prior to the onset of reconnection in the tail. The ion temperature was taken from the MHD results and the initial electron temperature was one fifth of the ion temperature. During the iPIC3D simulation the boundary conditions at the north and south boundaries were set by

using values from the MHD simulation, while those at the earthward and tail boundaries used free boundary conditions. The coupling is in one direction only, the PIC results do not feed back into the MHD calculation.

In Fig. 13 we show $B_{Z,}$ the component of the magnetic field normal to the equatorial plane, with the color coding at two times in the PIC simulation. In the top panel taken at 14 s just after fast reconnection starts the reconnection can be seen by the change from yellow to blue in the B_Z plot. A magnetic O region can be found just tailward of the x-point. In the bottom panel we show results from a snapshot taken 57 s into the simulation. A series of dipolarization fronts have formed and are propagating toward the Earth. They can be identified by yellow and red near the equator in the B_Z plot. The multiple dipolarization fronts form because of temporally varying reconnection (Ashour-Abdalla et al. 2014). Near the Earth the dipolarization fronts coalesce into thicker structures. Note that there are no dipolarization front-like signatures in the tailward region.

The reconnection process leads to electron heating. In Fig. 14 the perpendicular electron temperature has been plotted for four times. Early in the simulation when fast reconnection is just starting (15 s) there is very little heating. As the simulation progresses the heating occurs in the region near the north and south separatrices where temperature of the electrons exceeds 20 keV (see 44 s panel). There is less heating near the equator and even less near the X-point. For this simulation the highest temperatures were found in the southern hemisphere. Ashour-Abdalla et al. (2014) argue that the heating is mainly caused by a streaming instability in the separatrix region.

5 Reconnection and Turbulence

The role of turbulence is a recurring theme in studies of reconnection. In trying to anticipate where MMS will observe reconnection there are at least three aspects of such an investigation that appear to be important (Matthaeus and Velli 2011). First, even when starting from quiet equilibrium initial conditions, simulations of reconnection show clearly that turbulence is generated during the nonlinear evolution of the reconnection event. One such three-dimensional kinetic simulation is described in Daughton et al. (2011) and the argument that the simulation reflects the generation of intermittent cascading turbulence is discussed in Leonardis et al. (2013). Second, magnetofluid turbulence itself can give rise to reconnection (Matthaeus and Montgomery 1980; Matthaeus and Lamkin 1985; Servidio et al. 2011; Lazarian et al. 2012; Donato et al. 2013). The third way in which turbulence and reconnection are related occurs when the background within which reconnection is initiated is permeated by turbulence. In that situation, estimates of reconnection rates and classical pictures involving slow shock waves are likely to be modified dramatically by the background turbulence (Matthaeus and Lamkin 1985; Lazarian and Vishniac 1999; Kowal et al. 2009; Eyink et al. 2011; Lazarian et al. 2012). The turbulence can nudge fluid elements into thin current sheets and initiate reconnection. In addition, strong stochasticity is itself thought capable of effectively demagnetizing particle orbits, thus allowing the magnetic topology to change (i.e., reconnect) independent of the local resistivity (see, e.g., Eyink et al. 2011).

At present it is difficult to use existing spacecraft to study the question of whether or not turbulence is generated at sites of reconnection in geospace. The orbital separation of Cluster is generally too large to determine the three-dimensional statistical properties of the local magnetic fields. That situation will change with the MMS, which will have much closer separations and much higher time resolutions. What is clear, however, is that flows near presumed sites of reconnection are often populated by discontinuities and other fluctuations.

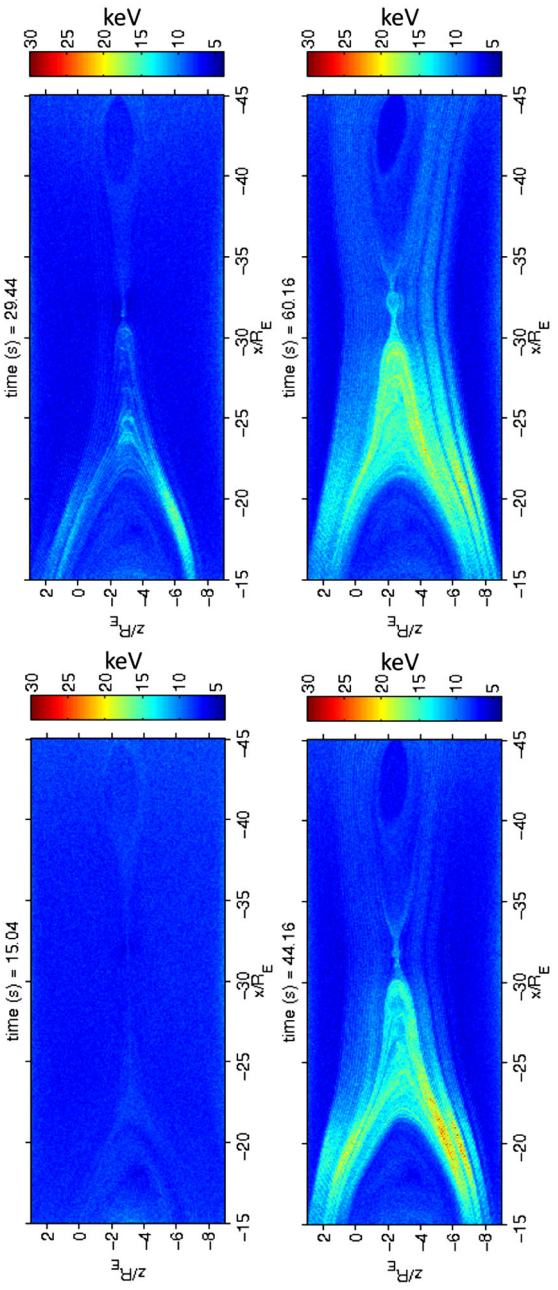

Fig. 14 The perpendicular temperature in keV at four times during the PIC simulation (from Ashour-Abdalla et al. 2014)

Such discontinuities can result from turbulence generated by reconnection as explored in the three-dimensional PIC simulation by Daughton et al. (2011) and Leonardis et al. (2013) and, as noted in the analyses of Cluster data, by Retinò et al. (2007) and Wendel and Adrian (2013). More easily addressed is the third aspect of the role of turbulence in magnetic reconnection, viz., the ubiquity of turbulence in many regions that show evidence of magnetic reconnection. The widespread presence of turbulence suggests that simple laminar initial conditions often employed in numerical studies of reconnection might not reflect accurately actual conditions to be encountered by MMS. The presence of turbulence in the magnetosheath results naturally from velocity shears and the convection of turbulence through the bow shock from the (turbulent) solar wind. The presence of that turbulence has been accounted for in the analyses of Cluster data discussed above. The situation in the magnetotail is more complex and less clear as most global simulations of the magnetosphere do not include turbulence in the initial conditions and, generally, do not generate turbulence as they evolve. However, there have been several analyses of magnetotail data and simulations of the magnetotail that have demonstrated the excitation of turbulence. We describe below some of our investigations of turbulence in the magnetotail using global MHD simulations.

The transport of magnetic flux, energy, and momentum in the magnetotail can be complex and variable even during quiet and steady magnetospheric conditions and is even more complex when the solar wind conditions are changing and the magnetosphere is in a disturbed state. The average convection in the plasma sheet is directed sunward on the earthward side of the reconnection region and tailward on the anti-sunward side of the reconnection region. Several studies (Borovsky et al. 1997; Angelopoulos et al. 1999; Chang et al. 1999a, 1999b; Klimas et al. 2000; Borovsky and Funsten 2003; Weygand et al. 2007) have presented evidence that turbulence in the plasma sheet plays a major role in the physics of the magnetotail.

At small scales, turbulence can contribute intermittently to the effective resistivity of the local plasma. At larger scales, turbulence can lead to the formation of multiple reconnection sites and flux tubes within current layers. Turbulence can significantly modify plasma transport properties, thereby altering the more global plasma dynamics involved in driving reconnection as well as provide a means by which particles can be accelerated to suprathermal energies. Boundary layers generated during reconnection produce turbulence that can then feed back on the reconnection process. At large scales in the plasma sheet, eddy turbulence is most likely generated in the sheared flows associated with localized fast flows driven by reconnection as described by Borovsky et al. (1997), Borovsky and Funsten (2003) (also see Weygand et al. 2005).

Reconnection in the plasma sheet has been described as an avalanching or cascading process (Uritsky et al. 2002, 2003; Klimas et al. 2004; Kozelov et al. 2004). A direct consequence of this is that reconnection in the plasma sheet at one position and time must be able to induce reconnection at a nearby site at a later time, which is the essence of an avalanche. Therefore plasma turbulence can be a link between reconnection sites. To help in understanding the specifics of reconnection onset and how this very local electron skin-depth phenomenon evolves to affect the plasma sheet, we have undertaken a series of global MHD simulations driven by constant or simplified solar wind/IMF conditions. These simulations produce magnetotail fluctuations with spectral properties similar to observations (El-Alaoui et al. 2010, 2011a, 2012). El-Alaoui et al. (2010, 2012) found power spectral densities (PSDs) and probability distribution functions (PDFs) that are consistent with in-situ observations and with theory. We found that localized reconnection was the main process driving turbulence.

The global MHD simulation showed that the magnetotail flows were far from laminar (El-Alaoui et al. 2010, 2011a, 2012). As an example, Fig. 15 shows snapshots taken

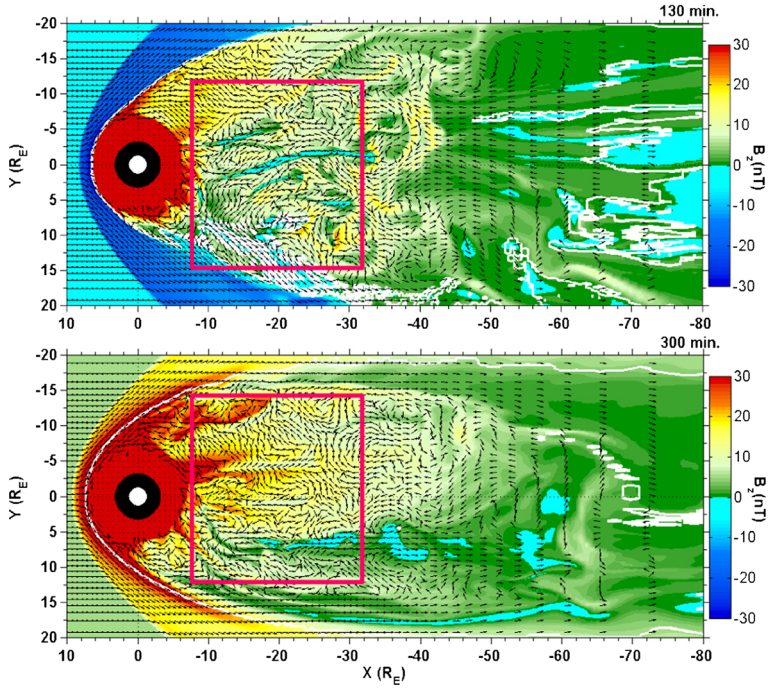

Fig. 15 Details of the equatorial plane showing flow vortices at 130 minutes (during southward IMF) and 300 minutes (during northward IMF) (from El-Alaoui et al. 2010)

at 130 minutes (during southward IMF) and 300 minutes (during northward IMF) into a generic run. Three variables are superimposed in the equatorial plane at each time. The color contours display the B_Z component of the magnetic field, the black arrows show flows in the plane and the white isocontours give the locations of the last closed field lines. Even though the IMF was uniformly southward, at 130 minutes the tail neutral line was highly variable and the B_Z distribution showed numerous meso-scale structures. In particular, at 90 minutes (not shown), a highly irregular reconnection region existed between $x = -30$ and $x = -60R_E$. At 130 minutes much of the reconnection was localized, extending only partway across the tail. Localized reconnection can be identified as a region of intense flow reversal, from earthward to tailward associated with reversals in the B_Z component of the magnetic field (white lines). The B_Z component is complex and includes filaments where B_Z is large and positive. A spacecraft encountering this type of filament would observe magnetic field changes resembling dipolarization. Distinct vortices are apparent in the figure. High-speed flows that encounter the near Earth region are deflected and form vortices of various sizes. This region is characterized by a strong magnetic field, hot plasma at the inner edge of the plasma sheet, and strong coupling to the ionosphere.

Smaller vortices are nested within the largest ones as can be seen by magnifying the region of the magenta box in Fig. 16. Several vortices exist in this box and some are indicated by grey ovals (Fig. 16a). This region is further magnified in Fig. 16b to reveal a yet smaller vortex nested in the larger one (Fig. 16c). Still smaller vortices exist. This pattern of nested vortices exists throughout the magnetotail during the simulation. The nested vortices in Fig. 16 and the variations in B_Z in Figs. 15 and 17 are both consistent with the presence of turbulence and a turbulent cascade.

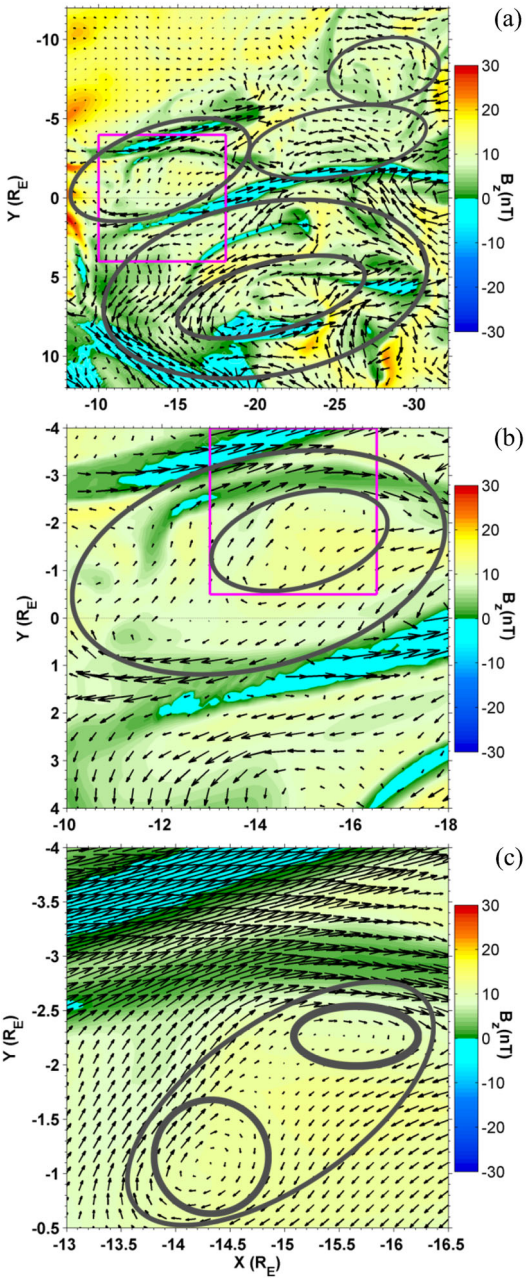

Fig. 16 B_Z color contours and flow vectors at 130 minutes in the equatorial plane. In the *top panel* the velocity vectors have been decimated by a factor of 5 in each direction. They have been decimated by a factor of 3 in each direction in the *middle panel*. All grid points are shown in the *lower panel* (from El-Alaoui et al. 2010)

In another global magnetohydrodynamic (MHD) simulation, El-Alaoui et al. (2009) found near-Earth flow vortices at the driving scale that agreed with magnetospheric observations taken at THEMIS P3 and P4. Around the time of substorm onset, flow vortices formed in the simulation near the locations of the two spacecraft, but the output was too sparse in space and time to resolve fully the turbulent spectrum. To verify that the flows were actually

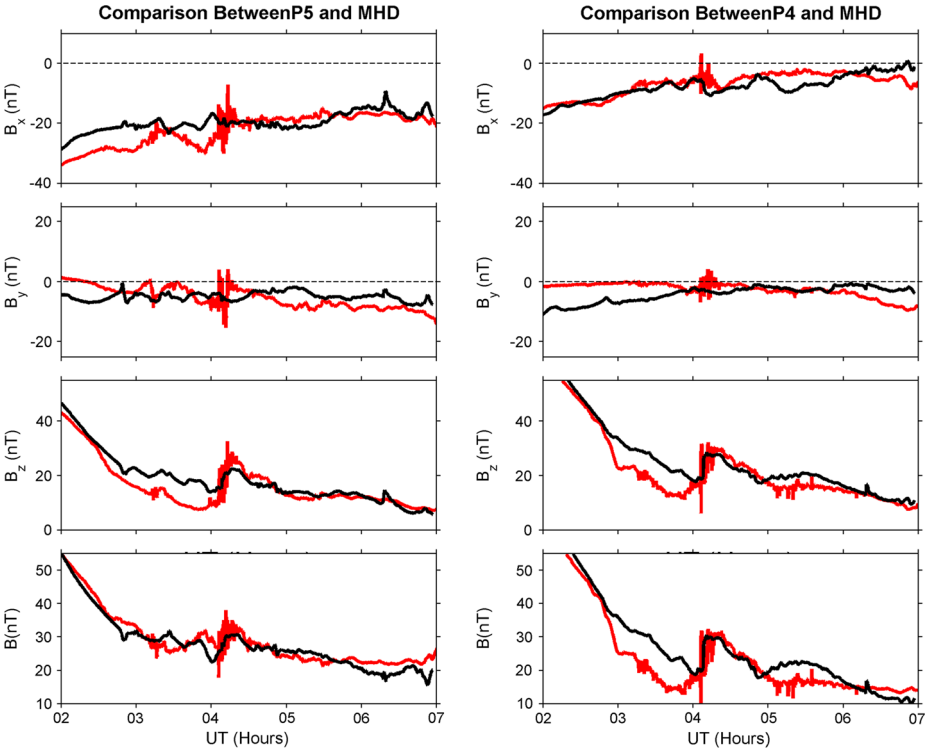

Fig. 17 A comparison of observed magnetic field time series (*red*) from THEMIS P5 (*left panels*) and THEMIS P4 (*right panels*) with global simulation results (*black*). Shown are the three components of B in GSE coordinates along with $|B|$ (after El-Alaoui et al. 2013)

turbulent, El-Alaoui et al. (2010, 2011b, 2012) extended the study via an event simulation driven by upstream solar wind observations with both high temporal and spatial resolution. The results indicated that the plasma sheet was turbulent (El-Alaoui et al. 2013).

The simulation reproduced not only the overall magnetotail changes observed by spacecraft, but also the observed spectral properties of the turbulence. The February 7, 2009 substorm event was chosen for the simulation because there were eight spacecraft located in different regions of the magnetosphere during the time of interest (0300 UT to 0500 UT). Wind spacecraft observations were used for the solar wind parameters. MHD output and THEMIS P4 magnetic field measurements from 0200 UT to 0700 UT are compared in Fig. 17 (right panels) (El-Alaoui et al. 2013). The passage of a strong dipolarization front near 0400 UT is prominent in both the observations and the simulation. The magnetic field observations at 3-second intervals are indicated in red. The black lines indicate MHD output at 20-second intervals.

Around 0400 UT, THEMIS P4 was within the dipolarized region as indicated by the time history of B_z. THEMIS P4 measured a value of B_x indicating that the spacecraft was located in the southern plasma sheet and was never close to the center of the current sheet. Important features in the observations also occur in the simulation. In particular, the timing and magnitude of the dipolarization front reflected in the B_z component were quite similar in the observations and in the simulation although the detailed behavior of fluctuations that lasted less than a few minutes were not possible to reproduce. THEMIS P5 saw develop-

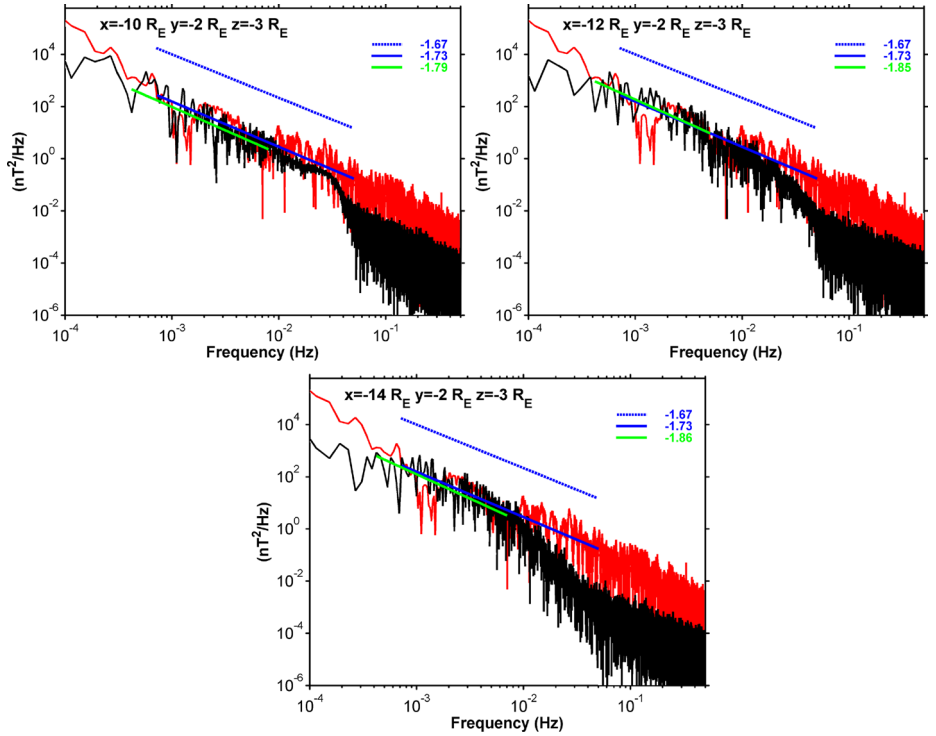

Fig. 18 The panels show PSDs for B_Z at the three locations in the MHD simulation listed in the panels (*black*) and at THEMIS P5 (*red*). The *solid blue* (*green*) *lines* are least squares fits in the inertial range for THEMIS data (MHD results). The *dashed blue lines*, shown for comparison, have the slopes of the theoretical prediction in the inertial range (from El-Alaoui et al. 2013)

ments similar to THEMIS P4 (Fig. 17 left panels). The magnetic field's y-component was relatively small and had an overall slow drift at both spacecraft that was reproduced by the simulation at both P4 and P5, with a better match at P4.

We tested the realism of the simulated turbulent spectra by comparing the PSDs calculated from observations at P5 with those at nearby locations in the simulation. PSDs of the north-south (z) component of the magnetic field were calculated from the simulation by using times between 0200 UT and 0500 UT, at $z = -3$ and $y = -2R_E$ for three x values: $-10R_E$, $-12R_E$, and $-14R_E$. The results are shown in Fig. 18. The driving, inertial and dissipative scales appear in both the observations and the simulation. A flat part of the spectrum in the MHD results appears at high frequencies as the MHD time-step size (typically between 0.01 and 0.1 s) is approached. The spectra show changes in the slope at transitions from one frequency range to the next (there are three ranges, driving, inertial and dissipative). At all three locations, the transitions occur at similar frequencies. The PSD slopes in the inertial and dissipative ranges were calculated by using least squares fits. Dashed lines with the $-5/3$ slope that characterizes fluid turbulence (Kolmogorov 1941) are included for comparison. The PSDs calculated from P5 measurements and from the simulations (Fig. 18) exhibited power levels in the driving and inertial ranges that were close enough for the traces to frequently overlap. The spectral indices in the inertial ranges are similar, with an observed index at P5 of -1.74 and indices in the simulation ranging from

-1.85 to -1.80. The breakpoints between the inertial and dissipative ranges appear to be close to 30 mHz.

The simulation results showed changes similar to those seen in the observed magnetic field and plasma flow during the event. Further, the simulation shows that PSDs and PDFs (not shown) computed from the simulation had the properties of fluid turbulence and that they were comparable to those seen in observations at THEMIS P5. The largest scales were associated with reconnection outflows that were diverted in the near-Earth region. The median value of the PSD slopes we obtained from event studies and in generic studies were close to $-5/3$ and both the PSD and PDF were comparable to those of Weygand et al. (2005).

These studies enhance our understanding of the relationship between turbulence and reconnection, especially in the magnetotail. MHD simulations have done a good job of generating turbulent spectra near dipolarization fronts. By comparing in situ observations to simulation results we hope to find out how the properties of turbulence depend on overall conditions. Eventually, MHD can be combined with kinetic studies to quantify the overall dissipation over both inertial and dissipative scales and how turbulence influences reconnection (Lapenta 2008; Kowal and Lazarian 2010; El-Alaoui et al. 2012, 2013). Studies using MMS data will probe further how turbulence changes the reconnection process and can affect the reconnection rate (Matthaeus and Lamkin 1985, 1986; Goldstein et al. 1986; Strauss 1988; Klimas et al. 2010; Eyink et al. 2011).

6 Summary

During the past several years, the GSFC-UCLA MOST IDS team has focused on several general themes. One activity has been to work with the FPI team in developing software tools to characterize the expected performance of both the DES and DIS detectors on orbit. In particular, we have helped to determine "burst mode triggers" that will flag data intervals of greatest scientific interest that will be telemetered to ground at the highest time resolution. This work included algorithms to account for various sources of error that affect the detection of particles as they move through the detectors. We also tested and developed various computational schemes for rapidly computing actual fluid moments from the electron and ion distribution functions (density, velocity, temperature, etc.).

The second general focus area has been to use Cluster and THEMIS data to explore in detail regions where reconnection has been observed so as to better characterize what MMS might encounter. On the dayside, we have used Cluster data when the four spacecraft were in a good tetrahedral configuration to characterize magnetic null geometry in the magnetosheath. The Cluster data were in general agreement with theories and descriptions of three-dimensional nulls. An interesting aspect of those data intervals is that they contained a significant level of magnetofluid turbulence.

In the magnetotail, the magnetic configuration resembles more the morphology of a Harris current sheet, but there, too, the data suggest a significant modification of any laminar picture due to the presence and generation of turbulence. Using both Cluster and THEMIS data, we characterized where and how particles are energized in the magnetotail. We found that particles were energized both adiabatically and nonadiabatically as dipolarization fronts swept up particles as the global magnetic fields relaxed toward more dipolar configurations or as particles bounced back and forth on moving field lines. For two quite similar events we were able to show, using global MHD, LSK and kinetic simulations why the observed particle characteristics were so distinct. We confirmed that although energization is associated

with and initiated by magnetic reconnection, the reconnection site is not necessarily where the strongest plasma heating and acceleration arise.

Turbulence generated by reconnection and turbulence affects how and where reconnection happens. The physical processes that trigger reconnection are influenced greatly by the ubiquity of turbulence in both the magnetosheath and magnetotail. Strong ambient turbulence appears capable of initiating reconnection if the magnetic and velocity fields are sufficiently stochastic. But as turbulence evolves in two and three dimensions, plasma bubbles can interact to form thin current sheets that become preferred sites of reconnection. Using global simulations to drive dipolarization fronts and magnetic substorms, we have shown that the excitation of reconnection in the tail current sheet is accompanied by the generation of strong turbulence that is characterized by nested vortical structures and power spectra that resemble Kolmogorov fluid turbulence.

References

V. Angelopoulos, W. Baumjohann, C.F. Kennel, F.V. Coronti, M.G. Kivelson, R. Pellat et al., J. Geophys. Res. **97**, 4027–4039 (1992)
V. Angelopoulos, C.F. Kennel, F.V. Coroniti, R. Pellat, M.G. Kivelson, R.J. Walker et al., J. Geophys. Res. **99**, 21257 (1994)
V. Angelopoulos, F.S. Mozer, T. Mukai, K. Tsuruda, S. Kokubun, T.J. Hughes, Geophys. Res. Lett. **26**, 2841–2844 (1999)
Y. Asano, I. Shinohara, A. Retinò, P.W. Daly, E.A. Kronberg, T. Takada et al., J. Geophys. Res. **115**, A05215 (2010)
M. Ashour-Abdalla, J.P. Berchem, J. Büchner, L.M. Zelenyi, J. Geophys. Res. **98**, 5651 (1993)
M. Ashour-Abdalla, M. El-Alaoui, V. Peroomian, R.J. Walker, L.M. Zelenyi, L.A. Frank et al., Geophys. Res. Lett. **26**, 3545–3548 (1999)
M. Ashour-Abdalla, M. El-Alaoui, F.V. Coroniti, R.J. Walker, V. Peroomian, Geophys. Res. Lett. **29**, 1965 (2002)
M. Ashour-Abdalla, M. El-Alaoui, M.L. Goldstein, M. Zhou, D. Schriver, R. Richard et al., Nat. Phys. **7**, 360–365 (2011)
M. Ashour-Abdalla, G. Lapenta, R. Walker, M. El-Alaoui, J. Geophys. Res. (2014, submitted)
G. Baumann, T. Haugbølle, A. Nordlund, Astrophys. J. **771**, 93 (2013)
W. Baumjohann, G. Paschmann, H. Luehr, J. Geophys. Res. **95**, 3801–3809 (1990)
J. Birn, E.R. Priest, in *Reconnection of Magnetic Fields* (Cambridge University Press, Cambridge, 2007)
J. Birn, J. Raeder, Y. Wang, R. Wolf, M. Hesse, Ann. Geophys. **22**, 1773–1786 (2004)
J. Birn, R. Nakamura, E.V. Panov, M. Hesse, J. Geophys. Res. **116**, 1210 (2011)
J.E. Borovsky, H.O. Funsten, J. Geophys. Res. Space Sci. **108**, 1284 (2003)
J.E. Borovsky, R.C. Elphic, H.O. Funsten, M.F. Thomsen, J. Plasma Phys. **57**, 1–34 (1997)
J. Büchner, L.M. Zeleny, Phys. Lett. A **118**, 395–399 (1986)
J. Büchner, L.M. Zelenyi, J. Geophys. Res. **94**, 11821–11842 (1989)
T. Chang, Astrophys. Space Sci. **264**, 303–316 (1999a)
T. Chang, Phys. Plasmas **6**, 4137–4145 (1999b)
L.-J. Chen, N. Bessho, B. Lefebvre, H. Vaith, A. Fazakerley, A. Bhattacharjee et al., J. Geophys. Res. **113**, 12213 (2008)
W. Daughton, V. Roytershteyn, H. Karimabadi, L. Yin, B.J. Albright, Nat. Phys. **7**, 539 (2011)
X. Deng, M. Ashour-Abdalla, M. Zhou, R. Walker, M. El-Alaoui, V. Angelopoulos et al., J. Geophys. Res. **115**, 12210 (2010a)
X. Deng, M. Ashour-Abdalla, M. Zhou, R. Walker, M. El-Alaoui, V. Angelopoulos et al., J. Geophys. Res. **115**, 09225 (2010b)
S. Donato, A. Greco, W.H. Matthaeus, S. Servidio, P. Dmitruk, J. Geophys. Res. Space Phys. **118**(7), 4033–4038 (2013)
S. Dubyagin, V. Sergeev, S. Apatenkov, V. Angelopoulos, R. Nakamura, J. McFadden et al., J. Geophys. Res. **115**, 10225 (2010)
J.P. Eastwood, M.A. Shay, T.D. Phan, M. Øieroset, Phys. Rev. Lett. **104**, 205001 (2010b)
J.P. Eastwood, T.D. Phan, M. Øieroset, M.A. Shay, J. Geophys. Res. **115**, 8215 (2010a)
J. Egedal, M. Øieroset, W. Fox, R.P. Lin, Phys. Rev. Lett. **94**, 25006 (2005)

J. Egedal, W. Fox, N. Katz, M. Porkolab, M. Øieroset, R.P. Lin et al., J. Geophys. Res. **113**, 12207 (2008)
J. Egedal, A. Lê, N. Katz, L.-J. Chen, B. Lefebvre, W. Daughton et al., J. Geophys. Res. **115**, A03214 (2010). doi:10.1029/2009JA014650
J. Egedal, W. Daughton, A. Lê, Nat. Phys. **8**, 321–324 (2012)
M. El-Alaoui, M. Ashour-Abdalla, R.J. Walker, V. Peroomian, R.L. Richard, V. Angelopoulos et al., J. Geophys. Res. **114**, A08221 (2009). doi:10.1029/2009JA014133
M. El-Alaoui, M. Ashour-Abdalla, R.L. Richard, M.L. Goldstein, J.M. Weygand, R.J. Walker, J. Geophys. Res. **115**, 12236 (2010)
M. El-Alaoui, M. Ashour-Abdalla, R.L. Richard, M.L. Goldstein, J.M. Weygand, R.J. Walker, J. Geophys. Res. **116**, A04206 (2011a)
M. El-Alaoui, R.L. Richard, M. Ashour-Abdalla, M.L. Goldstein, R.J. Walker, Ame. Geophys. Union **53**, 06 (2011b)
M. El-Alaoui, R.L. Richard, M. Ashour-Abdalla, R.J. Walker, M.L. Goldstein, Nonlinear Process. Geophys. **19**, 165–175 (2012)
M. El-Alaoui, R.L. Richard, M. Ashour-Abdalla, M.L. Goldstein, R.J. Walker, J. Geophys. Res. Space Phys. **118**, 7752–7761 (2013)
G.L. Eyink, A. Lazarian, E.T. Vishniac, Astrophys. J. **743**, 51 (2011)
H.S. Fu, Y.V. Khotyaintsev, M. André, A. Vaivads, Geophys. Res. Lett. **38**, 16104 (2011)
H.S. Fu, Y.V. Khotyaintsev, A. Vaivads, M. André, S.Y. Huang, Geophys. Res. Lett. **39**, 06105 (2012)
K. Fujimoto, Phys. Plasmas **13**, 2904 (2006)
D.J. Gershman et al., J. Geophys. Res. (2014, submitted)
M.V. Goldman, G. Lapenta, D.L. Newman, S. Markidis, H. Che, Phys. Rev. Lett. **107**, 135001 (2011)
M.L. Goldstein, W.H. Matthaeus, J.J. Ambrosiano, Geophys. Res. Lett. **13**, 205–208 (1986)
J.M. Greene, J. Comput. Phys. **98**, 194–198 (1992)
J.-S. He, C.-Y. Tu, H. Tian, C.-J. Xiao, X.-G. Wang, Z.-Y. Pu et al., J. Geophys. Res. **113**, A05205 (2008)
P.D. Henderson, C.J. Owen, A.D. Lahiff, I.V. Alexeev, A.N. Fazakerley, L. Yin et al., J. Geophys. Res. Space Phys. **113**, A07S31 (2008)
M. Hesse, K. Schindler, J. Geophys. Res. **93**, 5559–5567 (1988)
M. Hesse, T.G. Forbes, J. Birn, Astrophys. J. **631**, 1227–1238 (2005)
M. Hoshino, J. Geophys. Res. Space Phys. **110**, 10215 (2005)
M. Hoshino, T. Mukai, T. Terasawa, I. Shinohara, J. Geophys. Res. **106**, 25979–25998 (2001)
F.C. Huang, F.S. Wei, X.S. Feng, J. Plasma Phys. **72**, 1–10 (2006)
O.A. Hurricane, R. Pellat, F.V. Coroniti, Phys. Plasmas **3**, 2472–2474 (1996)
K.J. Hwang, M.L. Goldstein, E. Lee, J.S. Pickett, J. Geophys. Res. **116**, A00I32 (2011a)
K.J. Hwang, M.M. Kuznetsova, F. Sahraoui, M.L. Goldstein, E. Lee, G.K. Parks, J. Geophys. Res. **116**, 8210 (2011b)
K.J. Hwang, M.L. Goldstein, D.E. Wendel, A.N. Fazakerley, C. Gurgiolo, J. Geophys. Res. Space Phys. **118**, 4199–4209 (2013)
H. Karimabadi, W. Daughton, J. Scudder, Geophys. Res. Lett. **34**, 13104 (2007)
M.G. Kivelson, Eos **61**, 335 (1980)
A. Klimas, J.A. Valdivia, D. Vassiliadis, D.N. Baker, M. Hesse, J. Takalo, J. Geophys. Res. Space Phys. **105**, 18765 (2000)
A. Klimas, V.M. Uritsky, D. Vassiliadis, D.N. Baker, J. Geophys. Res. Space Phys. **109**, 2218 (2004)
A. Klimas, V. Uritsky, E. Donovan, J. Geophys. Res. Space Phys. **115**, 6202 (2010)
A.N. Kolmogorov, Dokl. Akad. Nauk SSSR **30**, 299 (1941)
G. Kowal, A. Lazarian, Astrophys. J. **720**, 742–756 (2010)
G. Kowal, A. Lazarian, E.T. Vishniac, K. Otmianowska-Mazur, Astrophys. J. **700**, 63–85 (2009)
B.V. Kozelov, V.M. Uritsky, A.J. Klimas, Geophys. Res. Lett. **31**, 20804 (2004)
D. Krauss-Varban, H. Karimabadi, Geophys. Res. Lett. **30**, 1308 (2003)
G. Lapenta, Phys. Rev. Lett. **100**, 235001 (2008)
G. Lapenta, S. Markidis, A. Divin, M. Goldman, D. Newman, Phys. Plasmas **17**, 2106 (2010)
G. Lapenta, S. Markidis, A. Divin, M.V. Goldman, D.L. Newman, Geophys. Res. Lett. **38**, L17104 (2011)
A. Lazarian, E.T. Vishniac, Astrophys. J. **517**, 700–718 (1999)
A. Lazarian, L. Vlahos, G. Kowal, H. Yan, A. Beresnyak, E.M. de Gouveia Dal Pino, Space Sci. Rev. **173**, 557–622 (2012)
A. Lê, J. Egedal, W. Daughton, W. Fox, N. Katz, Phys. Rev. Lett. **102**, 85001 (2009)
A. Lê, J. Egedal, O. Ohia, W. Daughton, H. Karimabadi, V.S. Lukin, Phys. Rev. Lett. **110**, 135004 (2013)
E. Leonardis, S.C. Chapman, W. Daughton, V. Roytershteyn, H. Karimabadi, Phys. Rev. Lett. **110**, 205002 (2013)
H. Liang, M. Ashour-Abdalla, R. Richard, D. Schriver, M. El-Alaoui, R.J. Walker, J. Geophys. Res. Space **119**, 5382–5400 (2014)

A.T.Y. Lui, Y. Zheng, Y. Zhang, S. Livi, H. Reme, M.W. Dunlop et al., Ann. Geophys. **24**, 2005–2013 (2006)
W. Lyatsky, M.L. Goldstein, Nonlinear Process. Geophys. **20**, 365–377 (2013)
S. Markidis, G. Lapenta, Rizwan-uddin, Math. Comput. Simul. **80**, 1509–1519 (2010)
W.H. Matthaeus, S.L. Lamkin, Phys. Fluids **28**, 303–307 (1985)
W.H. Matthaeus, S.L. Lamkin, Phys. Fluids **29**, 2513–2534 (1986)
W.H. Matthaeus, D.C. Montgomery, Selective decay hypothesis at high mechanical and magnetic Reynolds numbers, in *Nonlinear Dynamics*, vol. 357, ed. by H. Hellman (New York Academy of Sciences, New York, 1980), p. 203
W.H. Matthaeus, M. Velli, Space Sci. Rev. **160**, 145–168 (2011)
R. Nakamura, W. Baumjohann, B. Klecker, Y. Bogdanova, A. Balogh, H. Reme et al., Geophys. Res. Lett. **29**(20), 1942 (2002)
R. Nakamura, A. Retinò, W. Baumjohann, M. Volwerk, N. Erkaev, B. Klecker et al., Ann. Geophys. **27**, 1743–1754 (2009)
O. Ohia, J. Egedal, V.S. Lukin, W. Daughton, A. Lê, Phys. Rev. Lett. **109**, 115004 (2012)
S.-I. Ohtani, M.A. Shay, T. Mukai, J. Geophys. Res. Space Phys. **109**, 3210 (2004)
M. Øieroset, R.P. Lin, T.D. Phan, D.E. Larson, S.D. Bale, Phys. Rev. Lett. **89**, 195001 (2002)
Q. Pan, M. Ashour-Abdalla, R.J. Walker, M. El-Alaoui, J. Geophys. Res. Space Phys. **119**, 1060–1079 (2014)
C.E. Parnell, J.M. Smith, T. Neukirch, E.R. Priest, Phys. Plasmas **3**, 759–770 (1996)
T.D. Phan, T.E. Love, J.T. Gosling, G. Paschmann, J.P. Eastwood, M. Øieroset et al., Geophys. Res. Lett. **38**, 17101 (2011)
D.I. Pontin, G. Hornig, E.R. Priest, Geophys. Astrophys. Fluid Dyn. **98**, 407–428 (2004)
D.I. Pontin, G. Hornig, E.R. Priest, Geophys. Astrophys. Fluid Dyn. **99**, 77–93 (2005)
D.I. Pontin, A. Bhattacharjee, K. Galsgaard, Phys. Plasmas **14**, 052106 (2007)
D.I. Pontin, A.K. Al-Hachami, K. Galsgaard, Astron. Astrophys. **533**, A78 (2011)
E.R. Priest, P. Démoulin, J. Geophys. Res. **100**, 23443–23464 (1995)
E.R. Priest, D.I. Pontin, Phys. Plasmas **16**, 122101 (2009)
P.L. Pritchett, F.V. Coroniti, J. Geophys. Res. **115**, 06301 (2010)
A. Retinò, D. Sundkvist, A. Vaivads, F. Mozer, M. André, C.J. Owen, Nat. Phys. **3**, 236–238 (2007)
A. Runov, V. Angelopoulos, V.A. Sergeev, K.-H. Glassmeier, U. Auster, J. McFadden et al., Ann. Geophys. **27**, 319 (2009a)
A. Runov, V. Angelopoulos, M.I. Sitnov, V.A. Sergeev, J. Bonnell, J.P. McFadden et al., Geophys. Res. Lett. **36**, 14106 (2009b)
A. Runov, V. Angelopoulos, X.Z. Zhou, X.J. Zhang, S. Li, F. Plaschke et al., J. Geophys. Res. **116**, A05216 (2011)
C.T. Russell, R.L. McPherron, Space Sci. Rev. **15**, 205–266 (1973)
K. Schindler, M. Hesse, J. Birn, J. Geophys. Res. **93**, 5547–5557 (1988)
D. Schmid, M. Volwerk, R. Nakamura, W. Baumjohann, M. Heyn, Ann. Geophys. **29**, 1537–1547 (2011)
D. Schriver, M. Ashour-Abdalla, R.L. Richard, J. Geophys. Res. **103**, 14879 (1998)
D. Schriver, M. Ashour-Abdalla, L. Zelenyi, T. Gombosi, A. Ridley, D.D. Zeeuw et al., Modeling the kinetic transport of electrons through the Earth's global magnetosphere, in *Proceedings of the 7th ISSS (International School/Symposium for Space Simulations)* (RISH, Kyoto, 2005), pp. 345–346
J.D. Scudder, R.D. Holdaway, W.S. Daughton, H. Karimabadi, V. Roytershteyn, C.T. Russell et al., Phys. Rev. Lett. **108**, 225005 (2012)
V.A. Sergeev, R.C. Elphic, F.S. Mozer, A. Saint-Marc, J.-A. Sauvaud, Planet. Space Sci. **40**, 1551–1572 (1992)
V.A. Sergeev, V. Angelopoulos, S. Apatenkov, J. Bonnell, R. Ergun, R. Nakamura et al., Geophys. Res. Lett. **36**, 21105 (2009)
S. Servidio, P. Dmitruk, A. Greco, M. Wan, S. Donato, P.A. Cassak et al., Nonlinear Process. Geophys. **18**, 675–695 (2011)
M.A. Shay, J.F. Drake, J.P. Eastwood, T.D. Phan, Phys. Rev. Lett. **107**, 65001 (2011)
M.I. Sitnov, M. Swisdak, J. Geophys. Res. **116**, A12216 (2011)
M.I. Sitnov, M. Swisdak, A.V. Divin, J. Geophys. Res. **114**, A04202 (2009)
H.R. Strauss, Astrophys. J. **326**, 412–417 (1988)
D. Sundkvist, A. Retinò, A. Vaivads, S.D. Bale, Phys. Rev. Lett. **99**, 025004 (2007)
V.S. Titov, G. Hornig, P. Démoulin, J. Geophys. Res. Space Phys. **107**, 1164 (2002)
V.M. Uritsky, A.J. Klimas, D. Vassiliadis, Phys. Rev. E **65**, 46113 (2002)
V.M. Uritsky, A.J. Klimas, D. Vassiliadis, Geophys. Res. Lett. **30**, 1813 (2003)
A. Vaivads, A. Retinò, M. André, Space Sci. Rev. **122**, 19–27 (2006)
R. Wang, Q. Lu, X. Li, C. Huang, S. Wang, J. Geophys. Res. **115**, A11201 (2010)
D.E. Wendel, M.L. Adrian, J. Geophys. Res. Space Phys. **118**(4), 1571–1588 (2013)

D.E. Wendel, D.K. Olson, M. Hesse, N. Aunai, M. Kuznetsova, H. Karimabadi et al., Phys. Plasmas **20**, 122105 (2013)
J.M. Weygand, M.G. Kivelson, K.K. Khurana, H.K. Schwarzl, S.M. Thompson, R.L. McPherron et al., J. Geophys. Res. **110**, 01205 (2005)
J.M. Weygand, W.H. Matthaeus, S. Dasso, M.G. Kivelson, R.J. Walker, J. Geophys. Res. **112**, A10201 (2007)
M. Wiltberger, T.I. Pulkkinen, J.G. Lyon, C.C. Goodrich, J. Geophys. Res. **105**, 27649–27664 (2000)
R.A. Wolf, V. Kumar, F.R. Toffoletto, G.M. Erickson, A.M. Savoie, C.X. Chen et al., J. Geophys. Res. Space Phys. **111**, 12218 (2006)
R.A. Wolf, Y. Wan, X. Xing, J.C. Zhang, S. Sazykin, J. Geophys. Res. Space Phys. **114**, A00D05 (2009)
J.R. Wygant et al., J. Geophys. Res. Space Phys. **110**, A09206 (2005). doi:10.1029/2004JA010708
C.-J. Xiao, X.-G. Wang, Z.-Y. Pu, H. Zhao, J.X. Wang, Z.-W. Ma et al., Nat. Phys. **2**, 478–483 (2006)
M. Zhou, M. Ashour-Abdalla, X. Deng, D. Schriver, M. El-Alaoui, Y. Pang, Geophys. Res. Lett. **36**, 20107 (2009)
X.-Z. Zhou, V. Angelopoulos, V.A. Sergeev, A. Runov, J. Geophys. Res. Space Phys. **115**, A00I03 (2010). doi:10.1029/2010JA015481